Title: Gut bacterial metabolite imidazole propionate potentiates Alzheimer's disease pathology

Authors: Vaibhav Vemuganti[1,2†], Jea Woo Kang[3†], Qijun Zhang[1], Ruben Aquino-Martinez[1], Sandra Harding[3], Joseph Lawrence Harpt[1], Yuetiva Deming[3], Sterling Johnson[3,4], Sanjay Asthana[3,4], Henrik Zetterberg[3,5,6,7,8,9,10], Kaj Blennow[5,6,11,12] , Corinne D. Engelman[13], Tyler K. Ulland[3,14], Fredrik Bäckhed[15,16,17], Barbara B. Bendlin[3,4*], Federico E. Rey[1,18*]

Affiliations:

[1]Department of Bacteriology, University of Wisconsin-Madison; Madison, WI, USA.

[2]Cellular and Molecular Pathology Graduate Training Program, University of Wisconsin-Madison; Madison, WI, USA.

[3]Wisconsin Alzheimer's Disease Research Center, School of Medicine and Public Health, University of Wisconsin-Madison; Madison, WI, USA.

[4]Wisconsin Alzheimer's Institute, School of Medicine and Public Health, University of Wisconsin; Madison, WI, USA.

[5]Department of Psychiatry and Neurochemistry, Institute of Neuroscience and Physiology, the Sahlgrenska Academy at the University of Gothenburg; Mölndal, Sweden.

[6]Clinical Neurochemistry Laboratory, Sahlgrenska University Hospital; Mölndal, Sweden.

[7]Department of Neurodegenerative Disease, UCL Institute of Neurology; Queen Square, London, UK.

[8]UK Dementia Research Institute at UCL; London, UK.

[9]Hong Kong Center for Neurodegenerative Diseases; Inn,6,oHK, Hong Kong, China.

[10]Centre for Brain Research, Indian Institute of Science; Bangalore, India.

[11]Paris Brain Institute, ICM, Pitié-Salpêtrière Hospital, Sorbonne University; Paris, France.

[12]Neurodegenerative Disorder Research Center, Division of Life Sciences and Medicine, and Department of Neurology, Institute on Aging and Brain Disorders, University of Science and Technology of China and First Affiliated Hospital of USTC; Hefei, P.R. China.

[13]Department of Population Health Sciences, University of Wisconsin-Madison; Madison, WI, USA.

[14]Department of Pathology and Laboratory Medicine, University of Wisconsin-Madison; Madison, WI, USA.

[15]Wallenberg Laboratory, Department of Molecular and Clinical Medicine, University of Gothenburg; Gothenburg, Sweden.

[16]Region Västra Götaland, Sahlgrenska University Hospital, Department of Clinical Physiology; Gothenburg, Sweden.

[17]Microbiome Health Initiative and the National Food Institute, Technical University of Denmark; Kongens Lyngby, Denmark.

[18]Department of Medical Microbiology and Immunology, University of Wisconsin-Madison; Madison, WI, USA.

[†]These authors contributed equally to this work.

*Corresponding authors:

Federico E. Rey

ferey@wisc.edu

Barbara B. Bendlin

bbb@wisc.edu

One Sentence Summary

Gut bacterial metabolite increases dementia risk.

Abstract

The gut microbiome modulates metabolic, immune, and neurological functions and has been implicated in Alzheimer's disease (AD), though the specific mechanisms remain poorly defined. The bacterial metabolite imidazole propionate (ImP) has been previously associated with several AD comorbidities, such as type 2 diabetes and cardiovascular disease. Here, we show that elevated plasma ImP levels are associated with lower cognitive scores and AD biomarkers in a cohort of >1,100 cognitively unimpaired individuals. Metagenomic profiling identified gut bacteria encoding putative orthologs of the ImP-synthesizing enzyme, urocanate reductase (UrdA), whose abundance correlated with both cognitive measures and multiple AD biomarkers. Chronic ImP administration to mice activated neurodegenerative pathways, worsened AD-like neuropathology, and increased blood-brain barrier (BBB) permeability. Complementary *in vitro* studies showed that ImP compromised the integrity of human brain endothelial cells. Collectively, these findings implicate ImP in AD progression via both neurodegenerative and cerebrovascular mechanisms, identifying it as a potential target for early intervention.

Main Text:

INTRODUCTION

Alzheimer's disease (AD) is a progressive neurodegenerative disorder characterized by amyloid-β accumulation *(1)*, tau pathology *(2)*, and neuronal loss *(3, 4)*, as outlined in the amyloid, tau and neurodegeneration (ATN) framework *(5, 6)*. Aging and the apolipoprotein E (*APOE*) ε4 allele *(7, 8)* remain the most significant risk factors for AD *(7)*, but additional variables, including sex *(11, 12)*, body mass index (BMI) *(13)* modulate disease severity. Current estimates indicate that over 55 million people are living with dementia worldwide, with AD accounting for 60–70% of cases, and current treatment approaches focus on slowing disease progression or managing symptoms *(14)*. This underscores the need for the identification of novel, modifiable risk factors that can be detected and targeted earlier in the course of the disease.

Multiple lines of evidence suggest that alterations in the gut microbiota may precede or co-occur with AD pathology *(15–18)*. Gut microbes produce a wide range of metabolites that modulate host physiology and may influence disease progression *(16)*. Given the brain's reliance on systemic circulation *(19, 20)*, circulating gut microbiome-derived metabolites may influence central nervous system (CNS) function either indirectly via systemic effects or directly if they cross the blood-brain barrier (BBB). Previous studies have identified bacterial metabolites associated with AD *(16, 21)*, suggesting potential mechanistic links between gut microbial activity and neurodegeneration.

A recently discovered alternative pathway in histidine metabolism, mediated by the bacterial enzyme urocanate reductase (UrdA) produces imidazole propionate (ImP) *(22, 23)* during anaerobic respiration with urocanate as the electron acceptor *(24)*. Elevated circulating levels of ImP correlate with multiple AD-associated comorbidities, including type II diabetes *(25–28)*, hypertension *(29–31)*, atherosclerosis *(32)*, and chronic kidney disease *(33–36)*, suggesting potential detrimental effects on host health. In this study, we integrate cognitive assessments *(37)*, neuroimaging *(38)*, and multiomic *(37, 39)* analyses from the Wisconsin Alzheimer's Disease Research Center (ADRC), Wisconsin Registry for Alzheimer's Prevention (WRAP) *(40)* and Microbiome in Alzheimer's Risk Study (MARS) *(15, 41)* to investigate associations between circulating ImP, the abundance of bacteria encoding putative UrdA homologues, and

AD progression. Furthermore, we use two different transgenic mouse models that capture major aspects of AD pathology and *in vitro* cell culture models to explore causality. Our findings suggest that ImP contributes to neurovascular dysfunction and AD-related neuropathology.

RESULTS

Imidazole propionate (ImP) is associated with Alzheimer's disease and related dementias

Plasma levels of ImP measured in 1,196 cognitively unimpaired individuals from the Wisconsin ADRC and WRAP cohort *(40)* were matched with known AD covariates. Table 1 summarizes key demographic and clinical characteristics of the study cohort. Participants had a mean age of 61.2 years, were predominantly female (69%), and primarily White (94%). The average BMI was 29.2. *APOE* ε4 carrier status was positive in 38% of individuals.

Table 1. Participant demographics characterized for ImP levels.

	Overall, N = 1196 (100%)[1]
ImP	
Min, Max	−0.8, 1.3
Age	
Mean (SD)	61.2 (6.7)
Min, Max	39.4, 78.8
Sex	
Female	831 (69%)
Male	365 (31%)
Race	
American Indian or Alaska Native	14 (1.2%)
Asian	3 (0.3%)
Black or African American	41 (3.4%)
Other	13 (1.1%)
White	1,125 (94%)

***APOE* ε4 carrier status**	
Negative	737 (62%)
Positive	459 (38%)
BMI	
Mean (SD)	29.2 (6.4)

Abbreviations: ImP, Imidazole Propionate; SD, standard deviation; *APOE*, apolipoprotein E; BMI, body mass index.

[1]n (%).

Plasma ImP levels differed between females and males, with males showing elevated levels (**Fig. 1A**). We observed a significant positive relationship between age and ImP levels (**Fig. 1B**). We also examined the relationship between ImP and cognitive scores, while accounting for age, sex, BMI, *APOE* ε4 carrier status, and the age gap between plasma sample collection and cognitive performance assessment, using the ordinary least squares (OLS) multiple linear regression approach. All Preclinical Alzheimer's Cognitive Composite (PACC3) scores were significantly and negatively associated with levels of ImP ($P < 0.001$). Lower cognitive performance was associated with higher levels of plasma ImP while controlling for age and sex (**Fig. 1C**). Cognitive scores are often behavioral manifestations of underlying neuropathology. We observed a positive association between plasma levels of neurofilament light chain (NfL) ($\beta = 0.07$, $P = 0.00023$) (**Fig. 1D**) and phospho-Tau-217 (pTau-217) ($\beta = 0.09$, $P = 5.4e-05$) (**Fig. 1E**), which are robust markers of neurodegeneration *(42–44)*. Furthermore, stratifying by sex revealed a significant positive association between ImP and NfL in both sexes (**Fig. S1A**). However, the relationship between pTau-217 and ImP is only nearly significant in males ($\beta = 0.08$, $P = 0.056$) but significant in females ($\beta = 0.09$, $P = 0.0004$) **(Fig. S1B**). There was also a significant positive relationship between ImP and NfL measured in cerebrospinal fluid (CSF) (Spearman R=0.2; Adj. $P = 0.04$) (**Fig. S2A**). However, the association did not stand significant in the regression model after adjusting for age and sex. There was no significant relationship between ImP and [^{18}F]-fluorodeoxyglucose (FDG) standard uptake value ratio (SUVR) of the frontal, temporal, and parietal lobes (**Fig. S2B**). However, when stratified by sex, a significant negative association was detected in males for the frontal lobe ($\beta = -0.069$, $P = 0.043$) and parietal lobe ($\beta = -0.083$, $P = 0.037$), while no significant relationship was observed in the temporal lobe ($\beta = -0.04$, $P = 0.16$) (**Fig. 1F)** after controlling for age, BMI, *APOE* ε4 carrier status, and the age gap between sample collections. Altogether, these results identify multiple host factors that are associated with ImP levels in plasma and suggest novel associations with cognition and AD pathology.

Metagenome-assembled genomes (MAGs) encoding putative urocanate reductase are associated with Alzheimer's disease

We assessed the gut microbiome's capacity to generate ImP by quantifying the relative abundance of bacterial species harboring putative orthologs of the enzyme urocanate reductase (UrdA) and examined its association with AD biomarkers. We generated metagenome datasets from fecal samples (n=294) collected from individuals enrolled in the MARS cohort (**Table S1**). Sequencing data from each sample were individually assembled, and contigs clustered into metagenome-assembled genomes (MAGs), resulting in a total of 1,464 high-quality MAGs (>90% completeness and <5% contamination). We detected the presence of putative *urdA* orthologs in several MAGs including *Turicimonas muris, Eggerthella lenta, Faecalibacterium prausnitzii, Streptococcus mutans, Streptococcus pasteurianus, Duodenibacillus massiliensis, Lactobacillus paragasseri, Adlercreutzia hattorii, Sutterella wadsworthensis, Sutterella megalosphaeroides, Limosilactobacillus fermentum* and *Adlercreutzia equolifaciens* (**Fig. 2A**, **Fig. S3**) all of which were confirmed to have the tyrosine (Y) or methionine (M) residue at 373 in the FAD binding site, which are key for filtering enzyme specificity towards urocanate by excluding false positive hits for fumarate reductases *(22, 28, 45)* (**Fig. S4A)**. Some of these taxa have previously been identified as ImP producers *(24, 28, 31)*. We then applied multiple linear regression models to identify MAGs whose abundances were significantly associated with CSF biomarkers. MAGs positive for *urdA* were significantly associated with AD biomarkers, namely amyloid-β 42/40 ratio, α-synuclein, phosphorylated-tau (p-tau), and chitinase-3-like protein 1 (YKL-40) (**Fig. 2C**). Furthermore, *urdA*-positive MAGs from the genera *Limosilactobacillus, Lactobacillus* and *Streptococcus* were negatively associated with cognitive scores spread across the PACC3 tests (**Fig. 2B**). These results suggest that the abundance of gut bacterial taxa potentially harboring a key gene for ImP production is associated with AD. However, only *Duodenobacillus* was associated with pTau-217 and no *urdA* positive MAGs were significantly associated with plasma NfL or CSF NfL (**Fig. S4B, C**).

Imidazole propionate exacerbates neuropathology in Alzheimer's disease mouse models

To test whether ImP is causally related to the exacerbation of AD pathology, we examined whether increased levels of ImP influence AD pathology in two different mouse models that capture key features of AD, namely amyloid-β aggregation and tau pathology. We supplemented 5XFAD mice with ImP orally, via drinking water starting at 4 weeks of age, as previously reported *(32)*. This treatment was shown to increase plasma ImP *(32)*. We detected a significant increase in the number of amyloid-β plaques in the retrosplenial cortex of ImP-treated mice compared to their littermate controls consuming regular water (**Fig. 3A-D**). No differences were detected in the plaques' average volume and fluorescence intensity (**Fig. 3E, F**). Since amyloid-β plaques are closely associated with glial cells *(46)* , we examined astroglial reactivity in these mice. Sections stained for the reactive astrocyte marker GFAP showed a significantly higher number of $GFAP^+$ astrocytes in amyloid-β signal dense regions of the retrosplenial cortex (**Fig. 3B, C and G**).

We also examined the effect of elevating ImP in a tau pathology mouse model of AD. We supplemented PS19P301S mice with ImP in drinking water starting at 8 weeks of age. Brains were examined at 6 months of age to test whether ImP accelerates tau pathology in mice as cortical gliosis and tau accumulation were reported to be observed at this age *(47)*. Staining for the most commonly used monoclonal antibody p-tau AT-8 *(48)*, resulted in no distinct signal in the cortex and hippocampus in both groups. However, mice treated with ImP showed significantly higher astroglial reactivity within the piriform cortex, which is in stark contrast with the sparse populations of $GFAP^+$ glia detected in age-matched littermate controls (P = 0.0003) (**Fig. 4A-C**). Surprisingly, the reactive glia detected in both

groups of mice appeared to be morphologically different (**Fig. 4A, B)**. Thus, we used Sholl analysis *(49–51)* on cortical $GFAP^+$ glia to assess morphology. We observed that ImP-treated PS19P301S mice expressed increased process hypertrophy, indicating a more aggressive neuroimmune environment *(52, 53)* (**Fig. 4D, E**). This phenotype is not observed in 5XFAD mice (**Fig. 4F, G**), possibly due to glial reactivity being limited proximally to amyloid-β plaques, which are known to perturb homeostatic glia, contributing to their reactivity *(46, 54)*. Altogether, the results presented above strongly suggest that ImP exacerbates AD neuropathology in mice.

We performed proteomics and phosphoproteomics on cortical brain lysates from PS19P301S mice to identify potential alterations in p-tau and downstream tauopathy-associated pathways impacted by ImP, as it was shown to directly increase activation of p38γ *(55)* , which is a known kinase for tau at S202 and T205, the site which AT-8 binds to, and T181, the site at which AT-270 binds to on the mutant tau protein P301S 1N4R polypeptide sequence *(56)*. We identified 2352 unique proteins with 79 upregulated and 19 downregulated (fold change cut-off at 30%, FDR adj. $p<0.05$) proteins in cortices of ImP-treated mice compared to untreated littermate controls (**Fig. 5A**) (**Table S2**). Several proteins associated with reactive astrocytes such as GFAP, S100a1, S100a6 and S100b had increased abundances in ImP treated mice compared to untreated controls (**Table S2**), corroborating histopathological findings (**Fig. 4**). Enrichment analysis of proteins that are altered with a fold change >30% within ImP treated mice revealed pathway clusters associated with reactive oxygen species (ROS) stress and AD neuropathology (**Fig. 5B**). Further analysis on enriched pathways revealed several protein-protein interactions between enriched terms in pathways associated with mitochondrial function, axonal traffic, neuronal health and regulation of phosphorylation (**Fig. 5C**).

Follow-up phosphoproteomics analysis in these samples revealed 356 unique phosphorylated proteins with 7 upregulated and 2 downregulated (fold change cut-off at 30%, FDR adj. $p<0.05$) phospho-sites in ImP treated mice compared to untreated littermate controls (**Fig. 5D**) (**Table S3**). Furthermore, we tested for sequences within P301S-1N4R mutant tau to compare known phospho-sites modulated by several kinases, namely calcium-calmodulin dependent protein kinase II (CaMKII), cyclin-dependent kinase 5 (CDK-5), leucine-rich repeat kinase 2 (LRRK2), glycogen synthase kinase 3-beta (GSK3-B), protein kinase R (PKR), protein kinase A (PKA) and mitogen-activated protein kinases (MAPKs) under neurodegenerative conditions *(56–60)*. We specifically identified AA residues T153, T181, S202, T205, S208, T231 and S235 for their known roles in AD and related dementias (**Fig. 5E**) *(61, 62)*. Out of the phosphorylated residues, we detected >3-fold increase in phospho-T181 ($p<0.05$), also known as AT-270 which is associated with ADRD and a product of the MAPK p38γ- a previously reported target for ImP *(55)*. The other sites showed similar trends but did not reach significance. Combined, our results suggest that ImP may contribute to reactive gliosis by increasing tau phosphorylation, and inducing pathophysiological changes in neuronal, glial and mitochondrial crosstalk.

Imidazole propionate disrupts cerebrovascular integrity

For ImP to interact directly with cortical cells, it must either be transported across the endothelium into the CSF or diffuse into brain tissue following a neurovascular insult. Such entry likely requires blood-brain barrier (BBB) disruption, allowing ImP to access cortical regions with microvascular leakage. Notably, ImP has been shown to damage peripheral endothelial cells *(32)*, through mechanisms that may

also be relevant in the brain, potentially involving the glia limitans *(63)* a structure implicated in neurovascular injury responses. Glial reactivity often results from blood-brain barrier disruption *(64)* and vice versa *(65–67)*. To test whether the observed pathology in AD mice could be a result of direct cerebrovascular damage *(68–71)*, we examined vascular permeability using the Evans blue assay in C57Bl6J mice supplemented with ImP for 4 weeks. We found that ImP-treated mice accumulated higher levels of the dye in their brains compared to control animals, as determined by optical density (620nm) (**Fig. 6A**), indicating increased extravasation of Evans blue-bound albumin *(72)* into the brain tissue and potentially a leakier BBB in ImP-treated mice *(73)*.

Brain endothelial cells are key components of the BBB *(74)*; thus, we also examined the effect of ImP on the transepithelial electrical resistance and wound healing of primary human brain endothelial cells, as glia are known to influence the compounding or mitigation of cerebrovascular damage *(62–65)*. We found that levels of ImP within the range detected in humans (500 nM) *(27, 31, 32)* significantly reduced transepithelial electrical resistance (**Fig. 6B**) and the area invaded by regenerating endothelial cells in a wound healing assay (**Fig. 6C-E**). These results suggest that the effects of ImP on AD pathology may involve cerebrovascular mechanisms.

DISCUSSION

The findings presented here identify ImP as a potential early modifier of AD pathogenesis through both neurodegenerative and cerebrovascular mechanisms. Previous studies have established that gut microbiome alterations occur in individuals with AD *(15, 17, 18)*. Our study builds on this body of work by demonstrating that elevated plasma levels of the gut bacterial metabolite ImP are associated with lower cognitive performance in a large, mostly cognitively unimpaired cohort, and by providing causal evidence linking this metabolite with AD pathology in preclinical models. These results support the notion that microbial metabolites can influence host brain function well before clinical onset *(75)*. Moreover, the observed sex-specific associations with FDG-PET signal suggest ImP may contribute to early metabolic changes in the brain, in line with sex-dependent vulnerability to AD reported in other studies *(76–78)*.

We also extend prior work by linking ImP production to specific gut bacterial taxa. Previous research identified *E. lenta*, *S. wadsworthensis* and *A. equolifaciens* as ImP producers in metabolic disease contexts *(24, 27, 28, 31)*, and our metagenomic analysis confirms that these bacteria, along with others (**Fig. S4A**), harbor functional putative *urdA* homologs associated with adverse AD biomarker profiles. While earlier studies largely focused on the role of gut dysbiosis in modulating inflammation or neuropathology, our data expands the repertoire of microbial-derived neuroactive compounds implicated in AD *(16)*. Furthermore, these findings highlight that alterations microbial metabolism may drive disease-relevant phenotypes and offer specific intervention targets to change disease trajectory.

Using two complementary mouse models, we show that chronic ImP exposure worsens key features of AD pathology. In the tau model, these effects were accompanied by significant changes in the brain proteome and phosphoproteome, including increased abundance of reactive astrocyte markers and elevated phosphorylation of tau at disease-relevant residues. Mechanistically, our phosphoproteomic analysis indicates hyperactivation of kinases that regulate tau phosphorylation, which is known to destabilize neuronal microtubules *(79)*. In line with this, ImP-treated mice exhibited increased levels of tubulin monomers and decreased abundance of tubulin polymerization–promoting proteins, consistent

with impaired microtubule stability (**Table S2**). Notably, the protein transformer-2 protein homolog β (TRA2B), which is a known regulator of exon 10 splicing of tau associated with fronto-temporal dementia with Parkinsonism-17 (FTDP-17) *(80)* was among the most abundant proteins upregulated, potentially linking ImP to alternative splicing events relevant to tauopathies. This mechanism could potentially be controlled by serine/arginine repetitive matrix protein 1 (SRRM-1), which can bridge splicing machinery to enable TRA2B function in the production of pathogenic tau *(81)*. Furthermore, ImP-treated mice expressed higher levels of phosphorylated dynamin-1-like protein (DRP1) (**Table S3**), which is involved in mitochondrial fission *(82)*, potentially contributing to mitochondrial reactive oxygen stress marker upregulation in ImP treated mice (**Table S2**). Together, these results suggest that ImP not only exacerbates established AD pathologies but may also initiate broader neurodegenerative cascades involving glial activation, tau misprocessing, and cellular stress responses.

Lastly, we present evidence suggesting that ImP disrupts the integrity of BBB (**Fig. 6**). Previous work has shown that gut-derived molecules such as lipopolysaccharide (LPS) *(83)* and short-chain fatty acids (SCFAs) *(84–86)* can influence BBB permeability. Given mounting evidence that vascular and glial dysfunction is an early and independent contributor to AD *(20, 52, 53, 66, 68, 68, 87)*, our data suggest that microbial metabolites like ImP may act at the interface of metabolic, vascular, and neurodegenerative diseases. Together, our findings emphasize the need to consider gut bacterial metabolism as a modifiable factor in AD, with ImP as a potential risk factor and therapeutic target.

This study has several important limitations. First, our human cohort consisted primarily of cognitively unimpaired individuals from a single study site, which may limit the generalizability of our findings to broader or more diverse populations, including those with varying degrees of cognitive impairment or differing geographic and demographic backgrounds. However, two recent large studies associate ImP with cognitive decline, including the Medical Research Council (MRC) National Survey of Health of Development (NSHD) cohort (N = 1,740) *(88)* and the Rotterdam study (N = 1,082) *(89)*, with results matching our findings (**Fig. 1 and Fig. 2**). Second, the cross-sectional design precludes assessment of temporal or causal relationships. Longitudinal studies are needed to determine whether microbiome-derived metabolites, such as ImP, contribute to cognitive decline over time, although these would be difficult to perform due to the extended follow-up period needed. Third, while factors such as diet, lifestyle, medication use, and environmental exposures influence both cognitive health and gut microbiome composition, our data on these variables were limited, restricting our ability to control for their potential confounding effects. Future studies that include assessments of these factors are warranted.

Additionally, ImP was administered orally in preclinical studies. While this method effectively elevates plasma ImP levels *(32)*, it is essential to confirm our findings using gnotobiotic models colonized with microbial communities differing in ImP-producing capacity. Oral delivery *vs.* gut production may alter ImP kinetics and host responses. However, reproducible gnotobiotic models for ImP production remain under development. Lastly, in the 5XFAD model, which is sensitive to insulin signaling *(90)*, ImP's known effects on insulin signaling *(28)* may have contributed to the observed glial phenotype. Further studies are needed to clarify the molecular mechanisms linking ImP to AD pathophysiology.

Despite these limitations, the results presented here suggest ImP as a potential modifiable factor in the trajectory of Alzheimer's disease and potentially open up new avenues for microbiome-targeted interventions, such as modulation of ImP-producing taxa *(91)*, inhibition of UrdA enzymatic activity, or dietary strategies to limit histidine-to-ImP conversion *(92)*. As gut-brain axis research advances,

identifying and targeting specific microbial metabolic routes, like ImP production, may provide novel opportunities for early prevention or slowing of AD progression.

MATERIALS AND METHODS

Study design

The overall objective of this study is to test whether the gut-bacterial metabolite ImP is a potential risk factor for exacerbated disease outcomes in ADRD. Human subjects' data was obtained from WADRC, WRAP, and MARS cohorts, all of which are observational studies. The procedures for phenotype measurements are fully described in the corresponding Methods sections.

Experiments featuring transgenic pre-clinical murine models of AD are comprised of heterozygous transgenic mouse litters split into equal/nearly equal numbers of control and treatment groups. A final N = 4 was achieved per cage, with two different cages in each treatment group for a total of N = 8 mice per treatment group as two individual experiments. For PS19P301S mice, N = 4 mice/group were bred locally (using breeder obtained from Jackson labs), whereas the remaining 4 mice/group were purchased from Jackson Labs separately. Effect sizes were determined from previous studies to obtain an approximate N for the experiments. Mice were exposed to ImP chronically, via drinking water. One data point was excluded from **Fig. 6A** due to an abnormal amount of dye pooling at tissue level, post-mortem. The number of replicates used in histopathological analysis were mentioned in associated methods. All images were blinded using an in-house bash script, unblinded only for plotting the resultant data and obtaining representative images.

Participants

Participants were recruited from the ADRC and WRAP studies *(93)*. The Wisconsin ADRC clinical core recruits individuals representing the full clinical and biological spectrum of AD, ranging from cognitively unimpaired individuals to those with mild cognitive impairment and AD dementia. The WRAP is a longitudinal observational study that enrolls participants from a cohort enriched with individuals at increased risk for late-onset AD due to a parental history of AD dementia. Participants underwent *APOE* genotyping using competitive allele-specific PCR-based KASP™ assays (LGC Genomics, Beverly, MA) and participated in longitudinal assessments of cognitive function and laboratory tests. A subset of the cohort provided CSF samples collected via lumbar puncture and underwent PET neuroimaging to assess biomarkers of AD and related pathologies. Additionally, participants co-enrolled in the Microbiome in Alzheimer's Risk Study (MARS) provided fecal samples for gut microbiome analysis and completed questionnaires related to medical history and diet at the time of sample collection. Participants provided informed consent following the guidelines of the Declaration of Helsinki prior to enrollment in the Wisconsin ADRC, WRAP, and MARS studies. The study procedures were approved by the Institutional Review Board of the University of Wisconsin (Wisconsin ADRC and WRAP umbrella protocol ID: 2013-0178; MARS protocol ID: 2015-1121). Previous studies reported measurements of plasma ImP, PACC3 scores, CSF biomarkers, and FDG PET, and further methodological details are available in Supplementary Materials and Methods.

Metagenome Assembled Genomes and *urdA* gene annotation

Shotgun sequencing reads were assembled for all samples using SPAdes (v.3.15.5; metaspades.py -k 21,33,55,77), the assembled contigs were quantified by mapping shotgun reads to contigs using Bowtie2 (v.2.3.4). Contigs that were less than 500 bp were excluded for downstream analyses. Contigs were then binned into MAGs using MetaBAT2 (v.2.17). The quality of all MAGs was assessed by genome completeness and contamination using CheckM (v.1.2.2) and high-quality MAGs were kept (completeness > 90% and contamination < 5%). The high-quality MAGs were dereplicated using dRep (v.3.5.0; -pa 0.9 -sa 0.99). The final dataset contains 1464 MAGs. Taxonomic assignments of these 1464 MAGs were using the Genome Taxonomy Database Toolkit (GTDB-Tk; v.2.3.2) and the GTDB database (ver. R214). Genes from MAGs were predicted using Prodigal (v.2.6.3) and annotated to KEGG Orthology database using kofamscan (v.1.3.0) and annotated to Carbohydrate-Active Enzymes (CAZymes) database using dbcan3 (v.4.1.4) and database "dbCAN3_db_v12_20240415". MAGs were processed to create a single kallisto quantification index and reads from each faecal DNA sample were mapped to this index to quantify the abundance of each MAG in each sample *(94)*.

Hidden Markov model (HMM) was built using urdA reference genes from a collection of known ImP-producing bacteria *(28)*. Reference *urdA* gene sequences were aligned using MUSCLE (v.3.8.31) *(95)*, then the HMM profile was constructed using "hmmbuild" from HMMER (v.3.2.1). Protein coding genes (CDS) from MAGs were searched using HMM search (v.3.2.1). All genes involved exhibiting 60% score of the lowest scoring model sequence were included in subsequent analysis. Clustal Omega *(96)* was used for multiple alignment of predicted UrdA genes, and potential UrdA homologs (producing imidazole propionate from urocanate) were defined by "Y" or "M" residue at the FAD active sites tyrosine 373 (Y373).

Animal husbandry

All animals were obtained from The Jackson Laboratory, after which they were housed and bred in a specific-pathogen-free (SPF) facility at the University of Wisconsin-Madison. Male mice were split into cages of 4 with littermates evenly divided between test and control groups, and water intake was carefully monitored to obtain the average amount of water consumed per mouse within a cage for all cages. Imidazole propionate (Cayman Chemical) stock solution was prepared at 200µg/mL to match the average daily intake of water of mice at 4mL/day to enable a dosage of 800µg/mouse/day. Wild-type C57BL/6J mice were treated for 4 weeks before Evans blue extravasation assay and harvest. 5XFAD [B6.Cg-Tg(APPSwFlLon,PSEN1*M146L*L286V)6799Vas/Mmjax), Tg6799] mice were supplemented with ImP starting at 2 weeks of age until they were 6 months-old, whereas PS19P301S [B6;C3-Tg(Prnp-MAPT*P301S)PS19Vle/J] mice were treated starting at 8 weeks of age until they were 6 months-old. All protocols for this study were approved by the Institutional Animal Care and Use Committee (IACUC) at the University of Wisconsin-Madison.

Mouse brain sample collection and confocal microscopy

Mice were anesthetized with isoflurane [Isospire, Dechra] and blood was collected from the right ventricle. Mice were then perfused transcardiacally through the left ventricle with 15mL perfusion buffer consisting of PBS and heparin (0.5 USP). Brains were bisected into left and right hemispheres, where the left hemisphere was flash frozen and right hemisphere was fixed in 4% PFA for 48 hrs at 4C followed by fixation in 30% sucrose until the brains reach equal relative density to the sucrose solution. The brains were then fixed in sucrose [Fisher scientific] -OCT [Tissue-Tek, Sakura Finetek] solution for sectioning.

Brains were sectioned into 40µm sections from anterior to posterior and placed into an anti-freeze solution comprised of PBS [VWR Life science], sucrose and ethylene glycol [Sigma- Aldrich]. Sections from morphologically comparable regions with visible hippocampus, retrosplenial cortex and piriform cortex located 240µm apart from each other, were then washed with PBS and incubated with antibody for reactive astrocytes [GFAP (clone: GA5) 488 Conjugated, Invitrogen, 1:1000] for 12 hrs in 4C followed by another PBS wash and incubation with stain for amyloid-beta [MethOxy XO4, Tocris, 1:1000] and nuclei [TO-PRO-3 Iodide (642/661), ThermoFisher Scientific, 1:1000] at room temperature for 1 hour. The sections were then washed and mounted using a mounting solution [Fluoromount G, Invitrogen]. 3 images were taken from random regions within retrosplenial cortex in 5XFAD mice and piriform cortex in PS19P301S mice, from 3 different coronal sections using Zeiss LSM 800 (UW-Madison, Medical Microbiology and Immunology) and Nikon A1R microscopes (UW-Madison Biochemistry Optical Imaging Core).

Image analysis

Immunofluorescence data was quantified with the help of the surfaces and spots function on Imaris (Oxford Instruments). To count the number of GFAP+ cells, spots were generated with 6µm diameter localized to the center of astrocyte soma. Generated spots were cross-checked with spots generated by co-localizing nuclei with GFAP to obtain nuclei within GFAP+ areas as a proxy for cells. Surfaces function was used to render 3D solids using the amyloid-beta channel at fixed thresholds over all images, to render amyloid-beta plaques. A specialized MATLAB [Mathworks] script was used to separate individual plaques to obtain information on average volume, area and intensity. To quantify the hypertrophy in astrocyte processes, images were rendered on Image J (National Institutes of Health) where, 40µm thick hyper-stacks were converted into a 2D Z-project. A binary image was generated using the threshold feature, a region of interest was drawn around an isolated astrocyte and data outside the ROI was cleared. The skeletonize function was used to generate an astrocyte skeleton and we used SNT neuroanatomy plugin *(51)* set at 1µm intervals for Sholl analysis from the center of the skeleton up to 40µm away from the center.

Proteomics and phosphoproteomics

Proteins were extracted from flash-frozen cortices of PS19P301S male mice, followed by methanol-chloroform precipitation, tryptic/LysC digestion, and TMT labeling, as previously described (see Supplemental Methods). Phosphopeptides were enriched using sequential TiO□ and Zr-IMAC magnetic bead-based protocols and analyzed by nanoLC-MS/MS on an Orbitrap Fusion Lumos platform. Details provided in Supplemental Methods.

Evans blue extravasation assay

Mice were anesthetized as mentioned above, 1% Evans blue solution [Thermo Scientific] was prepared and filtered through 2µm syringe filter [Millipore]. 150uL of Evans blue solution was injected retro-orbitally and mice were allowed to recover for 30 minutes. Mice were anesthetized and perfused transcardiacally with perfusion buffer as mentioned above. Brains were collected, flash frozen and homogenized using a bead-beater with 0.1 mm zirconia beads [Biospec]. Homogenates were centrifuged at 10,000 RPM for 20 minutes at 4C, supernatant was collected, and absorbance was measured at 620nm. Final values were normalized by subtracting OD620 of a mouse brain without Evans blue treatment.

Cell culture assays

Human brain microvascular endothelial cells (HBMVEC) were purchased from iXCells Biotechnologies and grown in Endothelial Cell Growth Medium 2 and the corresponding supplements [PromoCell]. Cells were cultured in 5% CO2 at 37°C. Experiments were performed when cells reached confluency. HBMVEC were used between passage 4 and 6. Cells were treated with Imidazole Propionate at 500 nM through the growth medium. To evaluate wound healing, cells were cultured under normal conditions as above. At confluency, the monolayer was scratched with a P200 pipette tip in a plus (+) shape within the well and washed with PBS. The cells were imaged at 15 minutes, 3 hours and 24 hours. Images were analyzed on Image J by measuring percentage area invaded into the scratched region of interest. To test the membrane integrity, cells were cultured in transwell plates [Corning] with 500nM ImP within medium. TEER was measured using Electrical Resistance System and STX electrode [Millicell]. Final values were corrected for resistance of the blank membrane.

Statistical analysis

All statistical analysis on the human data was performed with Python (v3.12.1). The age difference between sample collections from two datasets was calculated for any dataset combined with plasma ImP data, and samples with an age difference greater than 4 years were filtered out. Mann–Whitney *U* test was used to analyze differences in ImP levels between females and males. Spearman correlation was performed to examine the relationship between age and ImP levels. These statistical analyses were performed with SciPy (v1.11.4). To test the relationship between ImP and cognitive performance, the ordinary least squares (OLS) multiple linear regression analysis was performed accounting for age, sex, BMI, *APOE* ε4 carrier status, and the age gap between plasma sample collection and assessment of cognitive performance using statsmodels (v0.14.1). The association between ImP and NFL, a CSF biomarker, Spearman correlation was performed using SciPy (v1.11.4). The relationship between ImP and FDG PET SUVR of the frontal lobe was determined with the OLS regression model using statsmodels (v0.14.1) adjusting for covariates including age, sex, BMI, *APOE* ε4 carrier status, and the age gap between plasma sample collection and FDG PET imaging. Multiple test correction was performed using the Benjamini–Hochberg procedure to control for false discovery rate using statsmodels (v0.14.1). All figures were generated using Matplotlib (v3.8.0) and seaborn (v0.13.2).

Multiple linear regression models were used to relate the abundances of MAGs with CSF biomarkers using the formula: *CSF biomarker ~ MAG + sex + age + BMI + APOE allele + NTK batch + age difference between fecal and CSF samples*. The alignment file generated using Clustal Omega was converted to FASTA format using the AlignIO.convert() function from Biopython (v1.85). Phylogenetic analysis was conducted using IQ-TREE with the MFP (Model Finder Plus) model, and bootstrap values were calculated with 1000 replicates (-bb 1000) and approximate likelihood ratio tests (ALRT) with 1000 replicates (-alrt 1000). The optimal number of threads was automatically determined (-nt AUTO). The resulting tree file was subsequently visualized and annotated using the Interactive Tree of Life (iTOL, v7.1) tool *(97)*.

The TPM (Transcripts per kilobase per million) output of kallisto followed by centered log ratio (CLT) transformation was used as MAG abundances in each sample. The beta coefficient for MAG from the formula was used to determine associations between CSF biomarkers with MAGs. Additionally corrected for batch effects from NTK samples using "*NTK batch*" covariate.

All statistical tests pertaining to mice and in vitro models are performed on GraphPad [PRISM v.10.3.1(509)]. Data was expressed in mean±SD or mean±s.e.m described under figure legends for appropriate graphs. Statistical significance was assessed utilizing two-tailed unpaired Student's *t*-tests, two-tailed Welch's *t*-test, Mann-Whitney U test or two-way repeated measures ANOVA, based on distribution of data points and differences standard deviation between test and control groups. The level of significance was set for P value<0.05.

Raw data pertaining to proteomics and phosphoproteomics was directly imported into Proteome Discoverer 3.1.0.638 where protein identifications and quantitative reporting was generated. Seaquest HT search engine platform with INFERYS rescoring-based workflow for high-resolution MS2 TMT quantification was used to interrogate Mus musculus (Mouse) reference proteome database (UP000000589, 04/19/2024 download, 54,874 total entries) containing human MAPT protein (P10636 UniProtKB accession). Peptide N-terminal and lysine TMT labeling plus Cysteine carbamidomethylation were selected as static modifications whereas methionine oxidation plus serine and threonine phosphorylation were selected as variable modifications. Peptide mass tolerances were set at 10ppm for MS1 and 0.03Da for MS2. Peptide and protein identifications were accepted under strict 1% FDR cut offs with high confidence XCorr thresholds of 1.9 for z=2 and 2.3 for z=3. For the total protein quantification processing Reporter Ion Quantifier settings were used on unique peptides, protein grouping was considered for uniqueness. Reporter abundance was based on normalized total peptide amount intensity values with co-isolation threshold filter set at ≤50. t-test (background based) hypothesis was executed without imputation mode being executed. For the phospho-enriched analysis no global normalization was applied, and only phosphorylated peptides were allowed for pairwise ratios quantification.

Acknowledgements

We extend our thanks to the WRAP and Wisconsin ADRC participants for their involvement and making this work possible. We thank the staff and researchers at the University of Wisconsin ADRC, the Wisconsin Alzheimer's Institute, the Wisconsin Institute for Medical Research, and the Waisman Center for their assistance in study organization, participant recruitment, and data collection, the University of Wisconsin Center for High Throughput Computing (CHTC) in the Department of Computer Sciences for providing computational resources, support and assistance.

Funding

Wisconsin Partnership Program grant (BBB, FER). National Institute on Aging Grants R01AG070973 (BBB, FER, TKU), R01AG083883 (TKU, BBB, FER), R21AG089348 (FER, BBB, TKU).
KB is supported by the Swedish Research Council (#2017-00915 and #2022-00732), the Swedish Alzheimer's Foundation (#AF-930351, #AF-939721, #AF-968270, and #AF-994551), Hjärnfonden, Sweden (#ALZ2022-0006, #FO2024-0048-TK-130 and #FO2024-0048-HK-24), the Swedish state under the agreement between the Swedish government and the County Councils, the ALF-agreement (#ALFGBG-965240 and #ALFGBG-1006418), the European Union Joint Program for Neurodegenerative Disorders (JPND2019-466-236), the Alzheimer's Association 2021 Zenith Award (ZEN-21-848495), the Alzheimer's Association 2022-2025 Grant (SG-23-1038904 QC), La Fondation Recherche Alzheimer (FRA), Paris, France, the Kirsten and Freddy Johansen Foundation, Copenhagen, Denmark, Familjen Rönströms Stiftelse, Stockholm, Sweden, and an anonymous filantropist and donor.

This study was in part supported by the Novo Nordisk Foundation (NNF24SA0092455; NNF Microbiome Health Initiative – from association to causality and novel management of cardiometabolic disease).Wallenberg Scholar and a Distinguished Professor at the Swedish Research Council supported by grants from the Swedish Research Council (#2023-00356, #2022-01018 and #2019-02397), the European Union's Horizon Europe research and innovation programme under grant agreement No 101053962, and Swedish State Support for Clinical Research (#ALFGBG-71320).

Author contributions

Conceptualization: VV, FB, BBB, FER
Methodology: VV, JWK, QZ, RAM, JLH, TKU
Investigation: VV, JWK, QZ, RAM
Visualization: VV, JWK, QZ
Funding acquisition: JWK, YD, SCJ, HZ, KB, CDE, TKU, BBB, FER
Project administration: BBB, FER
Supervision: BBB, FER
Writing – original draft: VV, JWK, BBB, FER
Writing – review & editing: VV, JWK, BBB, FER. All authors reviewed the manuscript.

Competing interests

KB has served as a consultant and at advisory boards for Abbvie, AC Immune, ALZPath, AriBio, Beckman-Coulter, BioArctic, Biogen, Eisai, Lilly, Moleac Pte. Ltd, Neurimmune, Novartis, Ono Pharma, Prothena, Quanterix, Roche Diagnostics, Sunbird Bio, Sanofi and Siemens Healthineers; has served at data monitoring committees for Julius Clinical and Novartis; has given lectures, produced educational materials and participated in educational programs for AC Immune, Biogen, Celdara Medical, Eisai and Roche Diagnostics; and is a co-founder of Brain Biomarker Solutions in Gothenburg AB (BBS), which is a part of the GU Ventures Incubator Program, outside the work presented in this paper. HZ has served at scientific advisory boards and/or as a consultant for Abbvie, Acumen, Alector, Alzinova, ALZpath, Amylyx, Annexon, Apellis, Artery Therapeutics, AZTherapies, Cognito Therapeutics, CogRx, Denali, Eisai, Enigma, LabCorp, Merck Sharp & Dohme, Merry Life, Nervgen, Novo Nordisk, Optoceutics, Passage Bio, Pinteon Therapeutics, Prothena, Quanterix, Red Abbey Labs, reMYND, Roche, Samumed, ScandiBio Therapeutics AB, Siemens Healthineers, Triplet Therapeutics, and Wave, has given lectures sponsored by Alzecure, BioArctic, Biogen, Cellectricon, Fujirebio, LabCorp, Lilly, Novo Nordisk, Oy Medix Biochemica AB, Roche, and WebMD, is a co-founder of Brain Biomarker Solutions in Gothenburg AB (BBS), which is a part of the GU Ventures Incubator Program, and is a shareholder of MicThera (outside submitted work).

Data and materials availability

All clinical data are available in previous publications mentioned in the respective methods section. The metagenomics dataset included in this study was deposited in the Sequence Read Archive (SRA) under accession number PRJNA1271016.

Figure Legends

Fig. 1. Plasma levels of Imidazole propionate are associated with lower cognitive scores and molecular markers of neurodegeneration. (**A**) Relationship between sex and plasma ImP levels (Mann–Whitney U test, ***P < 0.001). (**B**) ImP levels showed a positive correlation with age (Spearman). (**C**) Higher ImP levels were associated with lower cognitive performance across animal

naming, letter fluency, and trail-making test B using the OLS multiple linear regression model (controlling for age, sex, BMI, *APOE* ε4 carrier status, and the age gap between sample collections). Scatterplots with regression lines illustrate the relationships between (**D**) plasma NfL and ImP, and (**E**) pTau-217 and ImP. (**F**) Scatter plots with regression lines illustrate the relationship between plasma ImP and SUVR of the frontal, temporal and parietal lobes measured with FDG positron emission tomography (PET) in males (N = 51).

Fig. 2. Bacteria encoding putative urocanate reductase are associated with AD biomarkers in humans. (**A**) Section of a phylogenetic tree depicting the various MAGs within MARS cohort (N = 294). Each circular branch represents a species, with colors indicating the phylum to which each species belongs. The outer layer of the tree features boxes that depict the presence or absence of the *urdA* gene, with red-filled boxes representing gene presence and white boxes indicating gene absence. (**B**) Volcano plots displaying associations between abundances of *urdA*-harboring MAGs and PACC3 scores. (**C**) Volcano plots depicting several MAGs positive for *urdA* that are significantly associated with AD biomarkers.

Fig. 3. ImP exacerbates amyloid-beta pathology and reactive gliosis in 5XFAD male mice. (**A**) Representative images of brain sections from control (left) and ImP (right) treated mice, with nuclei (grey) and amyloid-beta (red) (scale bar = 1000µm). (**B, C**) Representative images of retrosplenial cortices of control and ImP-treated, stained for nuclei (grey), amyloid-beta (red) and reactive astrocytes (cyan) (scale bar = 200µm). (**D, E, F, G**) Immunofluorescence quantification (mean with SD, N = 8) of number of amyloid-beta plaques (P = 0.0001, unpaired t-test), average intensity per plaque (P > 0.05, unpaired t-test), average volume per plaque (P > 0.05, unpaired t-test with Welch's correction) and total number of GFAP+ astrocytes (P = 0.0006, Mann-Whitney U test).

Fig. 4. ImP accelerates cortical gliosis in PS19P301S male mice. (**A, B**) Representative images of reactive astrocytes (cyan) within piriform cortex of PS19P301S mice (nuclei, grey; scale bar = 100 µm). (**C**) Immunofluorescence-based quantification of reactive GFAP-positive astrocytes (mean with SD, n=8, P = 0.0003, Mann-Whitney U test). (**D**) Representative astrocyte skeletons from reactive astrocytes in piriform cortex of PS19P301S mice overlayed with concentric circles starting from center of soma, increasing radii by 1µm up to 40µm (scale bar = 40µm). (**E**) Quantification of morphological complexity (mean with SEM, N = 4) by Sholl analysis in PS19P301S (P < 0.0001, repeated measures two-way ANOVA). (**F**) Representative astrocyte skeletons from reactive astrocytes in retrosplenial cortex of 5XFAD mice overlayed with concentric circles starting from center of soma, increasing radii by 1µm up to 40µm (scale bar = 40µm). Arcs were digitally added to extend the empty concentric circles below ImP panel to aid visual symmetry. (**G**) Quantification of morphological complexity (mean with SEM, N = 4) by Sholl analysis in 5XFAD mice.

Fig. 5. ImP activates neurodegenerative signaling pathways in PS19P301S mice. (**A**) Volcano plot highlighting differentially expressed proteins in brain lysates from PS19P301S mice treated with ImP relative to control (FDR P <0.05, n=4 mice per treatment group; fold-change cut-off 30%). Red and blue denote increased and reduced abundances in ImP-treated mice, respectively. (**B**) Top 10 disease-associated pathways enriched among the differentially regulated proteins in ImP-treated mice. (**C**) Gene enrichment network visualizes clusters of proteins connected by direct or indirect interactions, organized by shared functional terms. Nodes are colored by enrichment term and their size scaled to the number of genes enriched under each term. For clarity, one term from each cluster is labeled using a color-matched

description. (**D**) Phosphoproteomic analysis. Volcano plot highlighting differentially phosphorylated proteins (FDR $P < 0.05$, N = 4 mice; cut-off 30%). (**E**) Phosphoprotein sequence hits for P301S-1N4R mutant were aligned to identify differential abundance of phosphorylated S and T amino acid residues (mean with SEM, N = 4). Aligned protein sequences, targeted phospho-AA residues, and respective kinases associated with phosphorylation at specific residues were listed under x-axis legends ($P<0.05$, unpaired t-test with Welch's correction).

Fig. 6. ImP treatment compromises cerebrovascular integrity. (**A**) Absorbance of brain homogenates from control and ImP-treated mice (n=5) following Evans blue injection (mean with SD, $P= 0.005$ unpaired t-test). (**B**) Quantification of TEER of human primary brain endothelial cells treated with 500nm ImP at 1hr (mean with SD, N = 5, $P = 0.01$, Mann-Whitney u test) and 24hrs (mean with SD, N = 5, $P = 0.06$, unpaired t-test). (**C**) Representative grayscale images of human primary brain endothelial cell monolayers in wound healing assay. (**D**) Quantification of percentage of wounded area being invaded by proliferating endothelial cells at 1hr (mean with SD, N = 5. $P = 0.06$, unpaired t-test with Welch's correction) and 3hrs (mean with SD, N = 5, $P = 0.02$, unpaired t-test).

Figure S1. Associations between plasma ImP and plasma biomarkers NfL and pTau-217 stratified by sex. (**A**) Scatterplots with regression lines illustrating relationship between plasma NfL and ImP, in males ($\beta = 0.10$, $P = 0.0072$) and females ($\beta = 0.06$, $P = 0.0098$). (**B**) Scatterplots with regression lines illustrating relationship between plasma pTau-217 and ImP, in males ($\beta = 0.08$, $P = 0.056$) and females ($\beta = 0.09$, $P = 0.00045$).

Figure S2. ImP is associated with CSF neurofilament light chain (NfL) and UrdA$^+$ MAGs are associated with negative cognitive test outcomes. (**A**) OLS regression for CSF biomarkers amyloid-β 42/40 ratio, α-synuclein, p-tau/amyloid-β 42 ratio, YKL-40, and NfL. (**B**) Scatter plots with regression lines illustrate the relationship between ImP and SUVR measured with FDG PET (N=167) for frontal, temporal and parietal lobes.

Figure S3. Metagenomic analysis reveals several *urdA* positive MAGs within the MARS cohort. (**A**) Phylogenetic tree depicting MAGs within MARS cohort (N = 294). Each circular branch represents a species, with colors indicating the phylum to which they belong. The outer layer of the tree features boxes depicting the presence (red box)/absence (white box) of the *urdA* gene.

Figure S4. Metagenomic analysis reveals several *urdA* positive MAGs within the MARS cohort II. (**A**) MAGs attributed with urdA have specific tyrosine (Y) or methionine (M) residue at 373rd position for substrate specificity to urocanate. (**B**) Volcano plots depicting associations between UrdA positive MAGs and plasma biomarkers, only *Duodenibacillus* is significantly associated with plasma pTau-217. However, the association does not withstand multiple hypothesis testing. (**C**) Several *urdA* positive MAGs trend positively with CSF NfL levels.

REFERENCES AND NOTES

1. H. Hampel, J. Hardy, K. Blennow, C. Chen, G. Perry, S. H. Kim, V. L. Villemagne, P. Aisen, M. Vendruscolo, T. Iwatsubo, C. L. Masters, M. Cho, L. Lannfelt, J. L. Cummings, A. Vergallo, The Amyloid-β Pathway in Alzheimer's Disease. *Mol Psychiatry* **26**, 5481–5503 (2021).

2. C. Ballatore, V. M.-Y. Lee, J. Q. Trojanowski, Tau-mediated neurodegeneration in Alzheimer's disease and related disorders. *Nat Rev Neurosci* **8**, 663–672 (2007).

3. M. J. West, P. D. Coleman, D. G. Flood, J. C. Troncoso, Differences in the pattern of hippocampal neuronal loss in normal ageing and Alzheimer's disease. *The Lancet* **344**, 769–772 (1994).

4. C. W. Cotman, J. H. Su, Mechanisms of Neuronal Death in Alzheimer's Disease. *Brain Pathology* **6**, 493–506 (1996).

5. H. Hampel, J. Cummings, K. Blennow, P. Gao, C. R. Jack, A. Vergallo, Developing the ATX(N) classification for use across the Alzheimer disease continuum. *Nat Rev Neurol* **17**, 580–589 (2021).

6. W. M. van der Flier, P. Scheltens, The ATN Framework—Moving Preclinical Alzheimer Disease to Clinical Relevance. *JAMA Neurology* **79**, 968–970 (2022).

7. Apolipoprotein E and Alzheimer disease., doi:10.1073/pnas.92.11.4725.

8. A. R. Roda, L. Montoliu-Gaya, S. Villegas, The Role of Apolipoprotein E Isoforms in Alzheimer's Disease. *Journal of Alzheimer's Disease* **68**, 459–471 (2019).

9. What Causes Alzheimer's Disease? | Alzheimer's Association*Alzheimer's Association* (available at https://www.alz.org/alzheimers-dementia/what-is-alzheimers/causes-and-risk-factors).

11. M. M. Mielke, Sex and Gender Differences in Alzheimer's Disease Dementia. *Psychiatr Times* **35**, 14–17 (2018).

12. E. M. Arenaza-Urquijo, R. Boyle, K. Casaletto, K. J. Anstey, C. Vila-Castelar, A. Colverson, E. Palpatzis, J. M. Eissman, T. Kheng Siang Ng, S. Raghavan, M. Akinci, J. M. J. Vonk, L. S. Machado, P. P. Zanwar, H. L. Shrestha, M. Wagner, S. Tamburin, H. R. Sohrabi, S. Loi, D. Bartrés-Faz, D. B. Dubal, P. Vemuri, O. Okonkwo, T. J. Hohman, M. Ewers, R. F. Buckley, for the Reserve, Resilience and Protective Factors Professional Interest Area, Sex and Gender Professional Interest area and the ADDRESS! Special Interest Group, Sex and gender differences in cognitive resilience to aging and Alzheimer's disease. *Alzheimer's & Dementia* **20**, 5695–5719 (2024).

13. S. Y. Kang, Y.-J. Kim, W. Jang, K. Y. Son, H. S. Park, Y. S. Kim, Body mass index trajectories and the risk for Alzheimer's disease among older adults. *Sci Rep* **11**, 3087 (2021).

14. Medications for Memory, Cognition & Dementia-Related Behaviors | alz.org*Alzheimer's Association* (available at https://www.alz.org/alzheimers-dementia/treatments/medications-for-memory).

15. N. M. Vogt, R. L. Kerby, K. A. Dill-McFarland, S. J. Harding, A. P. Merluzzi, S. C. Johnson, C. M. Carlsson, S. Asthana, H. Zetterberg, K. Blennow, B. B. Bendlin, F. E. Rey, Gut microbiome alterations in Alzheimer's disease. *Sci Rep* **7**, 13537 (2017).

16. J. W. Kang, V. Vemuganti, J. F. Kuehn, T. K. Ulland, F. E. Rey, B. B. Bendlin, Gut microbial metabolism in Alzheimer's disease and related dementias. *Neurotherapeutics* **21**, e00470 (2024).

17. Z.-Q. Zhuang, L.-L. Shen, W.-W. Li, X. Fu, F. Zeng, L. Gui, Y. Lü, M. Cai, C. Zhu, Y.-L. Tan, P. Zheng, H.-Y. Li, J. Zhu, H.-D. Zhou, X.-L. Bu, Y.-J. Wang, Gut Microbiota is Altered in Patients with Alzheimer's Disease. *Journal of Alzheimer's Disease* **63**, 1337–1346 (2018).

18. S. Liu, J. Gao, M. Zhu, K. Liu, H.-L. Zhang, Gut Microbiota and Dysbiosis in Alzheimer's Disease: Implications for Pathogenesis and Treatment. *Mol Neurobiol* **57**, 5026–5043 (2020).

19. N. A. Lassen, Cerebral Blood Flow and Oxygen Consumption in Man. *Physiological Reviews* **39**, 183–238 (1959).

20. C. Iadecola, Neurovascular regulation in the normal brain and in Alzheimer's disease. *Nat Rev Neurosci* **5**, 347–360 (2004).

21. N. M. Vogt, K. A. Romano, B. F. Darst, C. D. Engelman, S. C. Johnson, C. M. Carlsson, S. Asthana, K. Blennow, H. Zetterberg, B. B. Bendlin, F. E. Rey, The gut microbiota-derived metabolite trimethylamine N-oxide is elevated in Alzheimer's disease. *Alz Res Therapy* **10**, 124 (2018).

22. R. Venskutonytė, A. Koh, O. Stenström, M. T. Khan, A. Lundqvist, M. Akke, F. Bäckhed, K. Lindkvist-Petersson, Structural characterization of the microbial enzyme urocanate reductase mediating imidazole propionate production. *Nat Commun* **12**, 1347 (2021).

23. A. V. Bogachev, Y. V. Bertsova, D. A. Bloch, M. I. Verkhovsky, Urocanate reductase: identification of a novel anaerobic respiratory pathway in hewanella oneidensis MR-1. *Molecular Microbiology* **86**, 1452–1463 (2012).

24. A. S. Little, I. T. Younker, M. S. Schechter, P. N. Bernardino, R. Méheust, J. Stemczynski, K. Scorza, M. W. Mullowney, D. Sharan, E. Waligurski, R. Smith, R. Ramanswamy, W. Leiter, D. Moran, M. McMillin, M. A. Odenwald, A. T. Iavarone, A. M. Sidebottom, A. Sundararajan, E. G. Pamer, A. M. Eren, S. H. Light, Dietary- and host-derived metabolites are used by diverse gut bacteria for anaerobic respiration. *Nat Microbiol* **9**, 55–69 (2024).

25. W. L. Xu, E. von Strauss, C. X. Qiu, B. Winblad, L. Fratiglioni, Uncontrolled diabetes increases the risk of Alzheimer's disease: a population-based cohort study. *Diabetologia* **52**, 1031–1039 (2009).

26. L. Caberlotto, T.-P. Nguyen, M. Lauria, C. Priami, R. Rimondini, S. Maioli, A. Cedazo-Minguez, G. Sita, F. Morroni, M. Corsi, L. Carboni, Cross-disease analysis of Alzheimer's disease and type-2 Diabetes highlights the role of autophagy in the pathophysiology of two highly comorbid diseases. *Sci Rep* **9**, 3965 (2019).

27. A. Molinaro, P. Bel Lassen, M. Henricsson, H. Wu, S. Adriouch, E. Belda, R. Chakaroun, T. Nielsen, P.-O. Bergh, C. Rouault, S. André, F. Marquet, F. Andreelli, J.-E. Salem, K. Assmann, J.-P. Bastard, S. Forslund, E. Le Chatelier, G. Falony, N. Pons, E. Prifti, B. Quinquis, H. Roume,

S. Vieira-Silva, T. H. Hansen, H. K. Pedersen, C. Lewinter, N. B. Sønderskov, L. Køber, H. Vestergaard, T. Hansen, J.-D. Zucker, P. Galan, M.-E. Dumas, J. Raes, J.-M. Oppert, I. Letunic, J. Nielsen, P. Bork, S. D. Ehrlich, M. Stumvoll, O. Pedersen, J. Aron-Wisnewsky, K. Clément, F. Bäckhed, Imidazole propionate is increased in diabetes and associated with dietary patterns and altered microbial ecology. *Nat Commun* **11**, 5881 (2020).

28. A. Koh, A. Molinaro, M. Ståhlman, M. T. Khan, C. Schmidt, L. Mannerås-Holm, H. Wu, A. Carreras, H. Jeong, L. E. Olofsson, P.-O. Bergh, V. Gerdes, A. Hartstra, M. de Brauw, R. Perkins, M. Nieuwdorp, G. Bergström, F. Bäckhed, Microbially Produced Imidazole Propionate Impairs Insulin Signaling through mTORC1. *Cell* **175**, 947-961.e17 (2018).

29. A. Carey, S. Fossati, Hypertension and hyperhomocysteinemia as modifiable risk factors for Alzheimer's disease and dementia: New evidence, potential therapeutic strategies, and biomarkers. *Alzheimer's & Dementia* **19**, 671–695 (2023).

30. J. van Son, M. J. Serlie, M. Ståhlman, F. Bäckhed, M. Nieuwdorp, J. Aron-Wisnewsky, Plasma Imidazole Propionate Is Positively Correlated with Blood Pressure in Overweight and Obese Humans. *Nutrients* **13**, 2706 (2021).

31. A. Molinaro, I. Nemet, L. P. Bel, R. Chakaroun, T. Nielsen, -Wisnewsky Judith Aron, P.-O. Bergh, L. Li, M. Henricsson, øber L. K, R. Isnard, G. Helft, M. Stumvoll, O. Pedersen, J. G. Smith, W. H. W. Tang, ément K. Cl, S. L. Hazen, äckhed F. B, R. Alves, C. Amouyal, G. E. A. Andersson, F. Andreelli, O. Barthelemy, J.-P. Bastard, J.-P. Batisse, M. Berland, R. Bittar, üher M. Bl, P. Bork, O. Bourron, M. Camus, D. Cassuto, C. Ciangura, L. P. Coelho, J.-P. Collet, M.-E. Dumas, S. D. Ehrlich, L. Engelbrechtsen, L. Fezeu, S. Forslund, S. Fromentin, P. Galan, P. Giral, øtze J. P. G, T. Hansen, T. H. Hansen, A. Hartemann, B. Hartmann, S. Hercberg, B. Holmes, J. J. Holst, M. Hornbak, L. Hoyles, J.-S. Hulot, S. Jaqueminet, M. Kerneis, J. Khemis, R. Kozlowski, H. K. Pedersen, M. Kuhn, ås-H. L. Manner, L. Marko, -Gili Robin Massey Laura Martinez, N. Maziers, -Stamminger Jonathan Medina, -Silva Lucas Moitinho, G. Montalescot, S. Moutel, A. L. Neves, M. Olanipekun, J.-M. Oppert, C. Poitou, F. Pousset, L. Pouzoulet, C. Rouault, J. Silvain, H. Vestergaard, Microbially Produced Imidazole Propionate Is Associated With Heart Failure and Mortality. *JACC: Heart Failure* **11**, 810–821 (2023).

32. V. Nageswaran, A. Carreras, L. Reinshagen, K. R. Beck, J. Steinfeldt, M. Henricsson, P. Ramezani Rad, L. Peters, E. T. Strässler, J. Lim, B. J. H. Verhaar, Y. Döring, C. Weber, M. König, E. Steinhagen-Thiessen, I. Demuth, N. Kränkel, D. M. Leistner, M. Potente, M. Nieuwdorp, P. Knaus, W. M. Kuebler, M. Ferrell, I. Nemet, S. L. Hazen, U. Landmesser, F. Bäckhed, A. Haghikia, Gut Microbial Metabolite Imidazole Propionate Impairs Endothelial Cell Function and Promotes the Development of Atherosclerosis. *Arteriosclerosis, Thrombosis, and Vascular Biology* **45**, 823–839 (2025).

33. G. D. Stanciu, D. C. Ababei, V. Bild, W. Bild, L. Paduraru, M. M. Gutu, B.-I. Tamba, Renal Contributions in the Pathophysiology and Neuropathological Substrates Shared by Chronic Kidney Disease and Alzheimer's Disease. *Brain Sciences* **10**, 563 (2020).

34. S. E. O'Bryant, M. Petersen, J. Hall, L. A. Johnson, for the H.-H. S. Team, Medical comorbidities and ethnicity impact plasma Alzheimer's disease biomarkers: Important considerations for clinical trials and practice. *Alzheimer's & Dementia* **19**, 36–43 (2023).

35. D. Lv, W. Zheng, Z. Zhang, Z. Lin, K. Wu, H. Liu, X. Liao, Y. Sun, Microbial imidazole propionate affects glomerular filtration rate in patients with diabetic nephropathy through association with HSP90α. *Biochimica et Biophysica Acta (BBA) - Molecular Cell Research* **1871**, 119703 (2024).

36. Q. Chen, D. Ren, L. Liu, J. Xu, Y. Wu, H. Yu, M. Liu, Y. Zhang, T. Wang, Ginsenoside Compound K Ameliorates Development of Diabetic Kidney Disease through Inhibiting TLR4 Activation Induced by Microbially Produced Imidazole Propionate. *International Journal of Molecular Sciences* **23**, 12863 (2022).

37. E. M. Jonaitis, R. L. Koscik, L. R. Clark, Y. Ma, T. J. Betthauser, S. E. Berman, S. L. Allison, K. D. Mueller, B. P. Hermann, C. A. Van Hulle, B. T. Christian, B. B. Bendlin, K. Blennow, H. Zetterberg, C. M. Carlsson, S. Asthana, S. C. Johnson, Measuring longitudinal cognition: Individual tests versus composites. *Alzheimers Dement (Amst)* **11**, 74–84 (2019).

38. G. E. Ennis, A. Kohli, E. M. Jonaitis, T. J. Betthauser, J. M. Oh, C. E. Taylor, N. Chin, R. L. Koscik, B. T. Christian, S. Asthana, S. C. Johnson, B. B. Bendlin, The relationship of glucose-stimulated insulin secretion to cerebral glucose metabolism and cognition in healthy middle-aged and older adults. *Neurobiology of Aging* **105**, 174–185 (2021).

39. C. Van Hulle, E. M. Jonaitis, T. J. Betthauser, R. Batrla, N. Wild, G. Kollmorgen, U. Andreasson, O. Okonkwo, B. B. Bendlin, S. Asthana, C. M. Carlsson, S. C. Johnson, H. Zetterberg, K. Blennow, An examination of a novel multipanel of CSF biomarkers in the Alzheimer's disease clinical and pathological continuum. *Alzheimers Dement* **17**, 431–445 (2021).

40. S. C. Johnson, R. L. Koscik, E. M. Jonaitis, L. R. Clark, K. D. Mueller, S. E. Berman, B. B. Bendlin, C. D. Engelman, O. C. Okonkwo, K. J. Hogan, S. Asthana, C. M. Carlsson, B. P. Hermann, M. A. Sager, The Wisconsin Registry for Alzheimer's Prevention: A review of findings and current directions. *Alzheimer's & Dementia: Diagnosis, Assessment & Disease Monitoring* **10**, 130–142 (2018).

41. M. B. Heston, K. L. Hanslik, K. R. Zarbock, S. J. Harding, N. J. Davenport-Sis, R. L. Kerby, N. Chin, Y. Sun, A. Hoeft, Y. Deming, N. M. Vogt, T. J. Betthauser, S. C. Johnson, S. Asthana, G. Kollmorgen, I. Suridjan, N. Wild, H. Zetterberg, K. Blennow, F. E. Rey, B. B. Bendlin, T. K. Ulland, Gut inflammation associated with age and Alzheimer's disease pathology: a human cohort study. *Sci Rep* **13**, 18924 (2023).

42. Z. Xiao, W. Wu, X. Ma, J. Wu, X. Liang, X. Zhou, Y. Cao, Q. Zhao, D. Ding, Plasma p-tau217, p-tau181, and NfL as early indicators of dementia risk in a community cohort: The Shanghai Aging Study. *Alzheimer's & Dementia: Diagnosis, Assessment & Disease Monitoring* **15**, e12514 (2023).

43. N. J. Ashton, W. S. Brum, G. Di Molfetta, A. L. Benedet, B. Arslan, E. Jonaitis, R. E. Langhough, K. Cody, R. Wilson, C. M. Carlsson, E. Vanmechelen, L. Montoliu-Gaya, J. Lantero-Rodriguez, N. Rahmouni, C. Tissot, J. Stevenson, S. Servaes, J. Therriault, T. Pascoal, A. Lleó, D. Alcolea, J. Fortea, P. Rosa-Neto, S. Johnson, A. Jeromin, K. Blennow, H. Zetterberg, Diagnostic Accuracy of a Plasma Phosphorylated Tau 217 Immunoassay for Alzheimer Disease Pathology. *JAMA Neurology* **81**, 255–263 (2024).

44. N. J. Ashton, S. Janelidze, N. Mattsson-Carlgren, A. P. Binette, O. Strandberg, W. S. Brum, T. K. Karikari, F. González-Ortiz, G. Di Molfetta, F. J. Meda, E. M. Jonaitis, R. L. Koscik, K. Cody, T. J. Betthauser, Y. Li, E. Vanmechelen, S. Palmqvist, E. Stomrud, R. J. Bateman, H. Zetterberg, S. C. Johnson, K. Blennow, O. Hansson, Differential roles of Aβ42/40, p-tau231 and p-tau217 for Alzheimer's trial selection and disease monitoring. *Nat Med* **28**, 2555–2562 (2022).

45. A. V. Bogachev, Y. V. Bertsova, D. A. Bloch, M. I. Verkhovsky, Urocanate reductase: identification of a novel anaerobic respiratory pathway in Shewanella oneidensis MR-1. *Molecular Microbiology* **86**, 1452–1463 (2012).

46. D. R. Thal, The role of astrocytes in amyloid β-protein toxicity and clearance. *Experimental Neurology* **236**, 1–5 (2012).

47. Y. Yoshiyama, M. Higuchi, B. Zhang, S.-M. Huang, N. Iwata, T. C. Saido, J. Maeda, T. Suhara, J. Q. Trojanowski, V. M.-Y. Lee, Synapse Loss and Microglial Activation Precede Tangles in a P301S Tauopathy Mouse Model. *Neuron* **53**, 337–351 (2007).

48. M. Goedert, R. Jakes, E. Vanmechelen, Monoclonal antibody AT8 recognises tau protein phosphorylated at both serine 202 and threonine 205. *Neuroscience Letters* **189**, 167–170 (1995).

49. D. A. Sholl, Dendritic organization in the neurons of the visual and motor cortices of the cat. *J Anat* **87**, 387-406.1 (1953).

50. T. A. Ferreira, A. V. Blackman, J. Oyrer, S. Jayabal, A. J. Chung, A. J. Watt, P. J. Sjöström, D. J. van Meyel, Neuronal morphometry directly from bitmap images. *Nat Methods* **11**, 982–984 (2014).

51. C. Arshadi, U. Günther, M. Eddison, K. I. S. Harrington, T. A. Ferreira, SNT: a unifying toolbox for quantification of neuronal anatomy. *Nat Methods* **18**, 374–377 (2021).

52. R. Patani, G. E. Hardingham, S. A. Liddelow, Functional roles of reactive astrocytes in neuroinflammation and neurodegeneration. *Nat Rev Neurol* **19**, 395–409 (2023).

53. D. Kaur, V. Sharma, R. Deshmukh, Activation of microglia and astrocytes: a roadway to neuroinflammation and Alzheimer's disease. *Inflammopharmacol* **27**, 663–677 (2019).

54. M. Olsen, X. Aguilar, D. Sehlin, X. T. Fang, G. Antoni, A. Erlandsson, S. Syvänen, Astroglial Responses to Amyloid-Beta Progression in a Mouse Model of Alzheimer's Disease. *Mol Imaging Biol* **20**, 605–614 (2018).

55. A. Koh, L. Mannerås-Holm, N.-O. Yunn, P. M. Nilsson, S. H. Ryu, A. Molinaro, R. Perkins, J. G. Smith, F. Bäckhed, Microbial Imidazole Propionate Affects Responses to Metformin through p38γ-Dependent Inhibitory AMPK Phosphorylation. *Cell Metabolism* **32**, 643-653.e4 (2020).

56. V. Buée-Scherrer, M. Goedert, Phosphorylation of microtubule-associated protein tau by stress-activated protein kinases in intact cells. *FEBS Letters* **515**, 151–154 (2002).

57. P. R. Asih, K. Stefanoska, E. Prikas, A. Ittner, High Level Forebrain Expression of Active Tau Kinase p38γ Exacerbates Cognitive Dysfunction in Aged APP-transgenic Alzheimer's Mice. *Neuroscience* **484**, 53–65 (2022).

58. A. Ghosh, K. P. Giese, Calcium/calmodulin-dependent kinase II and Alzheimer's disease. *Molecular Brain* **8**, 78 (2015).

59. M. Hamm, R. Bailey, G. Shaw, S.-H. Yen, J. Lewis, B. I. Giasson, Physiologically relevant factors influence tau phosphorylation by leucine-rich repeat kinase 2. *Journal of Neuroscience Research* **93**, 1567–1580 (2015).

60. T. Li, C. Hawkes, H. Y. Qureshi, S. Kar, H. K. Paudel, Cyclin-Dependent Protein Kinase 5 Primes Microtubule-Associated Protein Tau Site-Specifically for Glycogen Synthase Kinase 3β. *Biochemistry* **45**, 3134–3145 (2006).

61. J. Neddens, M. Temmel, S. Flunkert, B. Kerschbaumer, C. Hoeller, T. Loeffler, V. Niederkofler, G. Daum, J. Attems, B. Hutter-Paier, Phosphorylation of different tau sites during progression of Alzheimer's disease. *Acta Neuropathologica Communications* **6**, 52 (2018).

62. P. Rawat, U. Sehar, J. Bisht, A. Selman, J. Culberson, P. H. Reddy, Phosphorylated Tau in Alzheimer's Disease and Other Tauopathies. *International Journal of Molecular Sciences* **23**, 12841 (2022).

63. P. Mora, P.-L. Hollier, S. Guimbal, A. Abelanet, A. Diop, L. Cornuault, T. Couffinhal, S. Horng, A.-P. Gadeau, M.-A. Renault, C. Chapouly, Blood–brain barrier genetic disruption leads to protective barrier formation at the Glia Limitans. *PLOS Biology* **18**, e3000946 (2020).

64. N. Marina, I. N. Christie, A. Korsak, M. Doronin, A. Brazhe, P. S. Hosford, J. A. Wells, S. Sheikhbahaei, I. Humoud, J. F. R. Paton, M. F. Lythgoe, A. Semyanov, S. Kasparov, A. V. Gourine, Astrocytes monitor cerebral perfusion and control systemic circulation to maintain brain blood flow. *Nat Commun* **11**, 131 (2020).

65. H. Kim, K. Leng, J. Park, A. G. Sorets, S. Kim, A. Shostak, R. J. Embalabala, K. Mlouk, K. A. Katdare, I. V. L. Rose, S. M. Sturgeon, E. H. Neal, Y. Ao, S. Wang, M. V. Sofroniew, J. M. Brunger, D. G. McMahon, M. S. Schrag, M. Kampmann, E. S. Lippmann, Reactive astrocytes transduce inflammation in a blood-brain barrier model through a TNF-STAT3 signaling axis and secretion of alpha 1-antichymotrypsin. *Nat Commun* **13**, 6581 (2022).

66. A. Verkhratsky, A. Butt, B. Li, P. Illes, R. Zorec, A. Semyanov, Y. Tang, M. V. Sofroniew, Astrocytes in human central nervous system diseases: a frontier for new therapies. *Sig Transduct Target Ther* **8**, 1–37 (2023).

67. O. Beylerli, I. Gareev, A. Beilerli, T. Ilyasova, H. Shi, A. Sufianov, The function of astrocytes in cerebral infarction and potential therapeutic approaches. *Brain Hemorrhages* **5**, 181–187 (2024).

68. W. Liu, A. Wong, A. C. K. Law, V. C. T. Mok, Cerebrovascular Disease, Amyloid Plaques, and Dementia. *Stroke* **46**, 1402–1407 (2015).

69. G. T. Stelzer, R. A. S. Lima-Filho, Amyloid-β as a Key Player in Cerebrovascular Dysfunction in Alzheimer's Disease. *J. Neurosci.* **44** (2024), doi:10.1523/JNEUROSCI.0663-24.2024.

70. E. Solis, K. N. Hascup, E. R. Hascup, Alzheimer's Disease: The Link Between Amyloid-β and Neurovascular Dysfunction. *J Alzheimers Dis* **76**, 1179–1198 (2020).

71. K. Honjo, S. E. Black, N. P. L. G. Verhoeff, Alzheimer's disease, cerebrovascular disease, and the β-amyloid cascade. *Can J Neurol Sci* **39**, 712–728 (2012).

72. R. A. Rawson, The binding of t-1824 and structurally related diazo dyes by the plasma proteins. *American Journal of Physiology-Legacy Content* **138**, 708–717 (1943).

73. Z. Guan, Q. Liu, Y. Wang, F. Xiao, G. Zhao, Relationship between tight junctions of the BBB and astrocyte connective function in epilepsy: Albumin and astrocyte activation. *Medicine Plus* **1**, 100047 (2024).

74. D. Wu, Q. Chen, X. Chen, F. Han, Z. Chen, Y. Wang, The blood–brain barrier: Structure, regulation and drug delivery. *Sig Transduct Target Ther* **8**, 1–27 (2023).

75. X.-N. Shen, J.-Q. Li, H.-F. Wang, H.-Q. Li, Y.-Y. Huang, Y.-X. Yang, L. Tan, Q. Dong, J.-T. Yu, A. D. N. Initiative, Plasma amyloid, tau, and neurodegeneration biomarker profiles predict Alzheimer's disease pathology and clinical progression in older adults without dementia. *Alzheimer's & Dementia: Diagnosis, Assessment & Disease Monitoring* **12**, e12104 (2020).

76. J.-C. Park, H. Lim, M. S. Byun, D. Yi, G. Byeon, G. Jung, Y. K. Kim, D. Y. Lee, S.-H. Han, I. Mook-Jung, Sex differences in the progression of glucose metabolism dysfunction in Alzheimer's disease. *Exp Mol Med* **55**, 1023–1032 (2023).

77. S. P. Caminiti, C. Boccalini, N. Nicastro, V. Garibotto, D. Perani, Sex differences in brain metabolic connectivity architecture in probable dementia with Lewy bodies. *Neurobiology of Aging* **126**, 14–24 (2023).

78. B. Feng, J. Cao, Y. Yu, H. Yang, Y. Jiang, Y. Liu, R. Wang, Q. Zhao, Gender-Related Differences in Regional Cerebral Glucose Metabolism in Normal Aging Brain. *Front Aging Neurosci* **14**, 809767 (2022).

79. D. N. Drechsel, A. A. Hyman, M. H. Cobb, M. W. Kirschner, Modulation of the dynamic instability of tubulin assembly by the microtubule-associated protein tau. *MBoC* **3**, 1141–1154 (1992).

80. Z. Jiang, H. Tang, N. Havlioglu, X. Zhang, S. Stamm, R. Yan, J. Y. Wu, Mutations in Tau Gene Exon 10 Associated with FTDP-17 Alter the Activity of an Exonic Splicing Enhancer to Interact with Tra2β*. *Journal of Biological Chemistry* **278**, 18997–19007 (2003).

81. M. Chen, J. L. Manley, Mechanisms of alternative splicing regulation: insights from molecular and genomics approaches. *Nat Rev Mol Cell Biol* **10**, 741–754 (2009).

82. S. C. Kamerkar, F. Kraus, A. J. Sharpe, T. J. Pucadyil, M. T. Ryan, Dynamin-related protein 1 has membrane constricting and severing abilities sufficient for mitochondrial and peroxisomal fission. *Nat Commun* **9**, 5239 (2018).

83. W. A. Banks, A. M. Gray, M. A. Erickson, T. S. Salameh, M. Damodarasamy, N. Sheibani, J. S. Meabon, E. E. Wing, Y. Morofuji, D. G. Cook, M. J. Reed, Lipopolysaccharide-induced blood-brain barrier disruption: roles of cyclooxygenase, oxidative stress, neuroinflammation, and elements of the neurovascular unit. *Journal of Neuroinflammation* **12**, 223 (2015).

84. V. Braniste, M. Al-Asmakh, C. Kowal, F. Anuar, A. Abbaspour, M. Tóth, A. Korecka, N. Bakocevic, L. G. Ng, P. Kundu, B. Gulyás, C. Halldin, K. Hultenby, H. Nilsson, H. Hebert, B. T. Volpe, B. Diamond, S. Pettersson, The gut microbiota influences blood-brain barrier permeability in mice. *Science Translational Medicine* **6**, 263ra158-263ra158 (2014).

85. J. Xie, A. Bruggeman, C. De Nolf, C. Vandendriessche, G. Van Imschoot, E. Van Wonterghem, L. Vereecke, R. E. Vandenbroucke, Gut microbiota regulates blood□cerebrospinal fluid barrier function and Aβ pathology. *The EMBO Journal* **42**, e111515 (2023).

86. E. G. Knox, M. R. Aburto, C. Tessier, J. Nagpal, G. Clarke, C. M. O'Driscoll, J. F. Cryan, Microbial-derived metabolites induce actin cytoskeletal rearrangement and protect blood-brain barrier function. *iScience* **25**, 105648 (2022).

87. I. Farhy-Tselnicker, N. J. Allen, Astrocytes, neurons, synapses: a tripartite view on cortical circuit development. *Neural Dev* **13**, 7 (2018).

88. R. Green, J. Lord, J. Xu, J. Maddock, M. Kim, R. Dobson, C. Legido-Quigley, A. Wong, M. Richards, P. Proitsi, Metabolic correlates of late midlife cognitive outcomes: findings from the 1946 British Birth Cohort. *Brain Communications* **4**, fcab291 (2022).

89. S. Ahmad, T. Wu, M. Arnold, T. Hankemeier, M. Ghanbari, G. Roshchupkin, A. G. Uitterlinden, J. Neitzel, R. Kraaij, C. M. V. Duijn, M. A. Ikram, R. Kaddurah-Daouk, G. Kastenmüller, the A. D. M. Consortium, The blood metabolome of cognitive function and brain health in middle-aged adults – influences of genes, gut microbiome, and exposome, 2024.12.16.24317793 (2024).

90. W. Chen, Q. Huang, E. K. Lazdon, A. Gomes, M. Wong, E. Stephens, T. G. Royal, D. Frenkel, W. Cai, C. R. Kahn, Loss of insulin signaling in astrocytes exacerbates Alzheimer-like

phenotypes in a 5xFAD mouse model. *Proceedings of the National Academy of Sciences* **120**, e2220684120 (2023).

91. H. Mitsunobu, Y. Kita, Y. Nambu-Nishida, S. Miyazaki, K. Nakajima, K. Taoka, A. Kondo, K. Nishida, Development of a highly efficient base editing system for Lactobacilli to improve probiotics and dissect essential functions, 2024.08.12.607654 (2024).

92. Y. Nishimoto, Y. Mizuguchi, Y. Mori, M. Ito, S. Miyazato, Y. Kishimoto, T. Yamada, S. Fukuda, Resistant Maltodextrin Intake Reduces Virulent Metabolites in the Gut Environment: A Randomized Control Study in a Japanese Cohort. *Front. Microbiol.* **13** (2022), doi:10.3389/fmicb.2022.644146.

93. S. C. Johnson, R. L. Koscik, E. M. Jonaitis, L. R. Clark, K. D. Mueller, S. E. Berman, B. B. Bendlin, C. D. Engelman, O. C. Okonkwo, K. J. Hogan, S. Asthana, C. M. Carlsson, B. P. Hermann, M. A. Sager, The Wisconsin Registry for Alzheimer's Prevention: A review of findings and current directions. *Alzheimers Dement (Amst)* **10**, 130–142 (2017).

94. L. Schaeffer, H. Pimentel, N. Bray, P. Melsted, L. Pachter, Pseudoalignment for metagenomic read assignment. *Bioinformatics* **33**, 2082–2088 (2017).

95. R. C. Edgar, MUSCLE: multiple sequence alignment with high accuracy and high throughput. *Nucleic Acids Research* **32**, 1792–1797 (2004).

96. F. Sievers, A. Wilm, D. Dineen, T. J. Gibson, K. Karplus, W. Li, R. Lopez, H. McWilliam, M. Remmert, J. Söding, J. D. Thompson, D. G. Higgins, Fast, scalable generation of high□quality protein multiple sequence alignments using Clustal Omega. *Molecular Systems Biology* **7**, 539 (2011).

97. I. Letunic, P. Bork, Interactive Tree of Life (iTOL) v6: recent updates to the phylogenetic tree display and annotation tool. *Nucleic Acids Research* **52**, W78–W82 (2024).

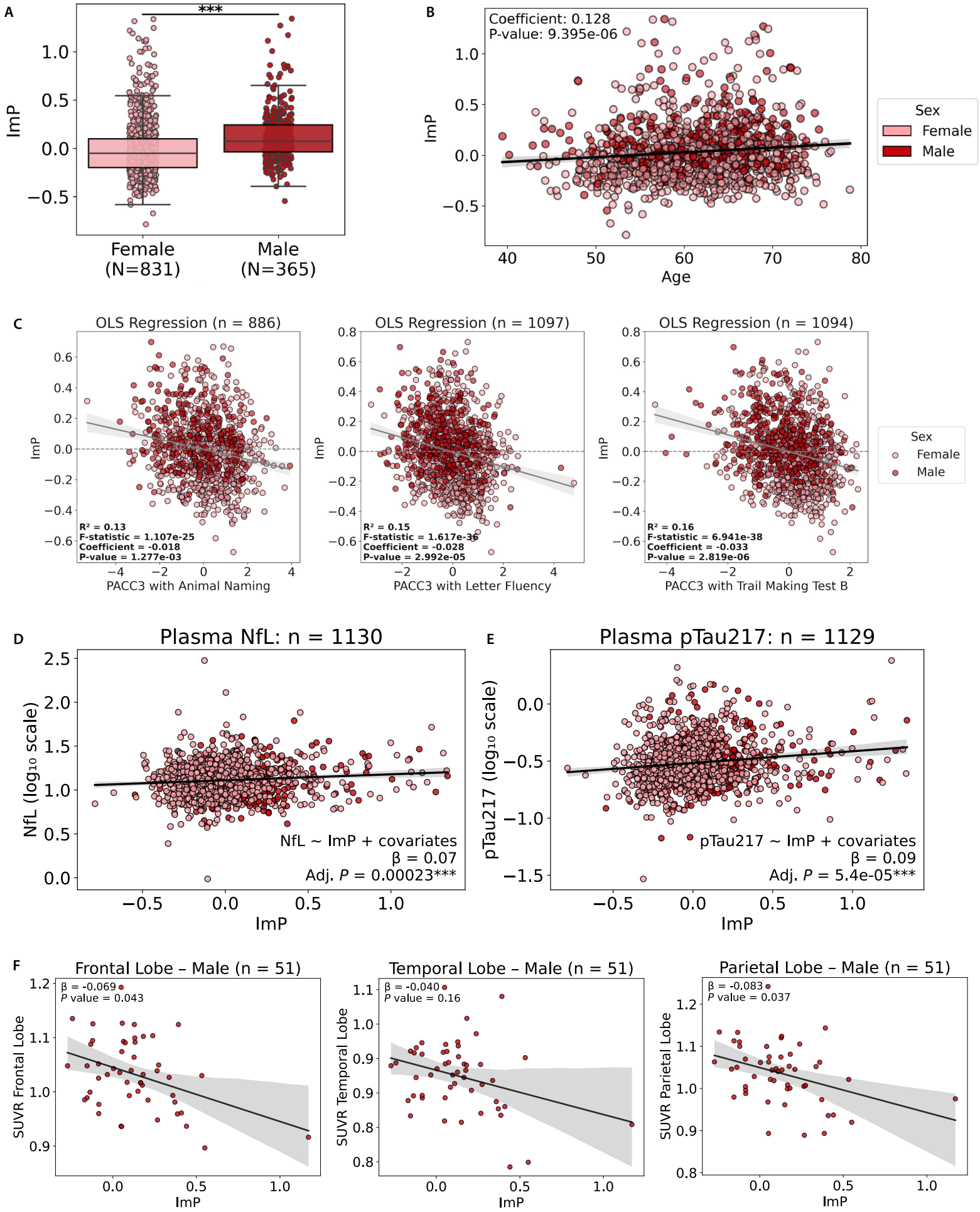
A
***
ImP
Female (N=831)
Male (N=365)
B
Coefficient: 0.128
P-value: 9.395e-06
ImP
Age
Sex
Female
Male
C
OLS Regression (n = 886)
R² = 0.13
F-statistic = 1.107e-25
Coefficient = -0.018
P-value = 1.277e-03
PACC3 with Animal Naming
OLS Regression (n = 1097)
R² = 0.15
F-statistic = 1.617e-36
Coefficient = -0.028
P-value = 2.992e-05
PACC3 with Letter Fluency
OLS Regression (n = 1094)
R² = 0.16
F-statistic = 6.941e-38
Coefficient = -0.033
P-value = 2.819e-06
PACC3 with Trail Making Test B
Sex
Female
Male
D
Plasma NfL: n = 1130
NfL (log10 scale)
NfL ~ ImP + covariates
β = 0.07
Adj. P = 0.00023***
ImP
E
Plasma pTau217: n = 1129
pTau217 (log10 scale)
pTau217 ~ ImP + covariates
β = 0.09
Adj. P = 5.4e-05***
ImP
F
Frontal Lobe – Male (n = 51)
β = -0.069
P value = 0.043
SUVR Frontal Lobe
ImP
Temporal Lobe – Male (n = 51)
β = -0.040
P value = 0.16
SUVR Temporal Lobe
ImP
Parietal Lobe – Male (n = 51)
β = -0.083
P value = 0.037
SUVR Parietal Lobe
ImP

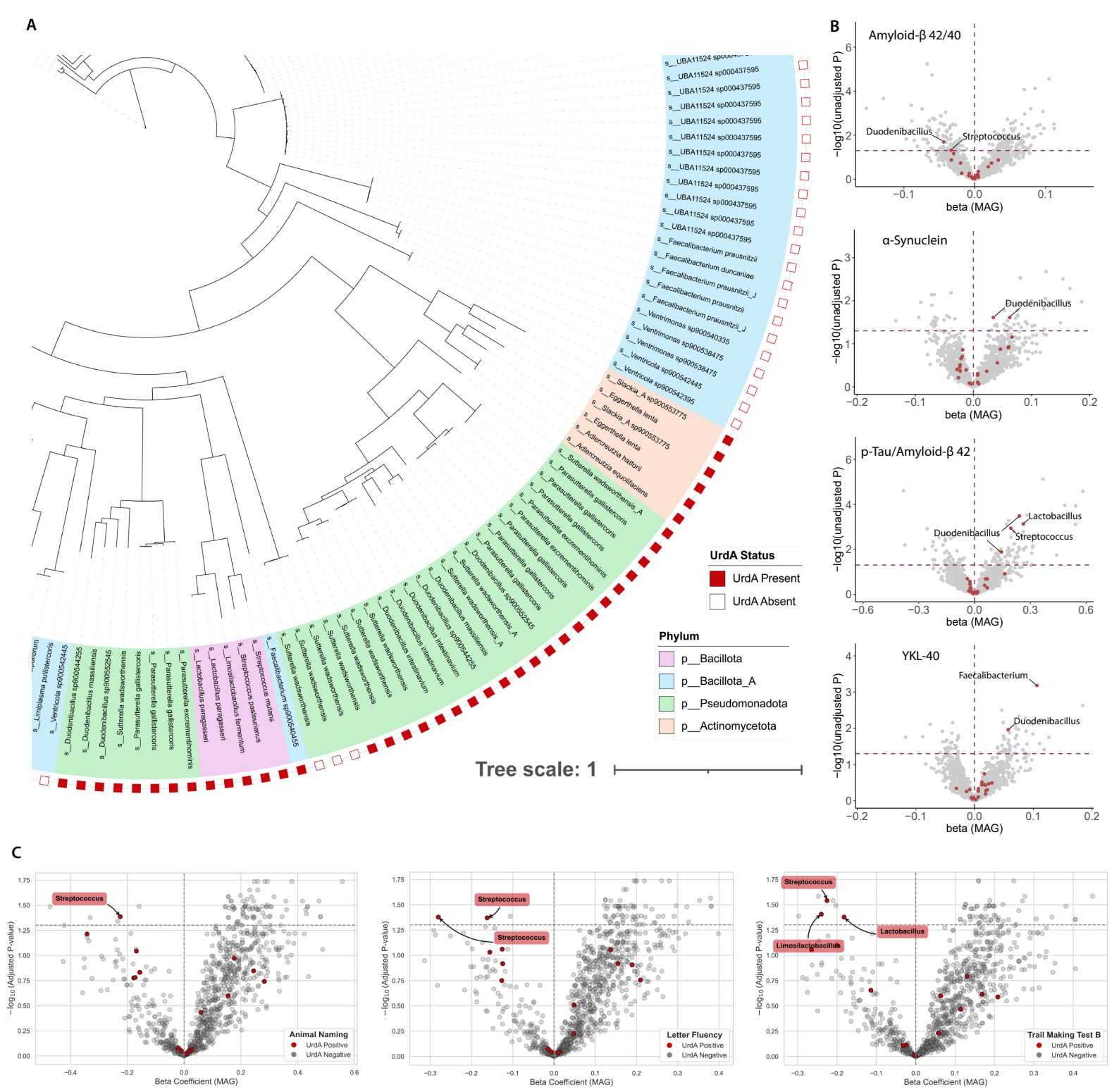
A
UrdA Status
UrdA Present
UrdA Absent
Phylum
p__Bacillota
p__Bacillota_A
p__Pseudomonadota
p__Actinomycetota
Tree scale: 1
B
Amyloid-β 42/40
Duodenibacillus
Streptococcus
α-Synuclein
Duodenibacillus
p-Tau/Amyloid-β 42
Lactobacillus
Duodenibacillus
Streptococcus
YKL-40
Faecalibacterium
Duodenibacillus
−log10(unadjusted P)
beta (MAG)
C
Streptococcus
Animal Naming
UrdA Positive
UrdA Negative
Letter Fluency
Trail Making Test B
Lactobacillus
Limosilactobacillus
−log10 (Adjusted P-value)
Beta Coefficient (MAG)

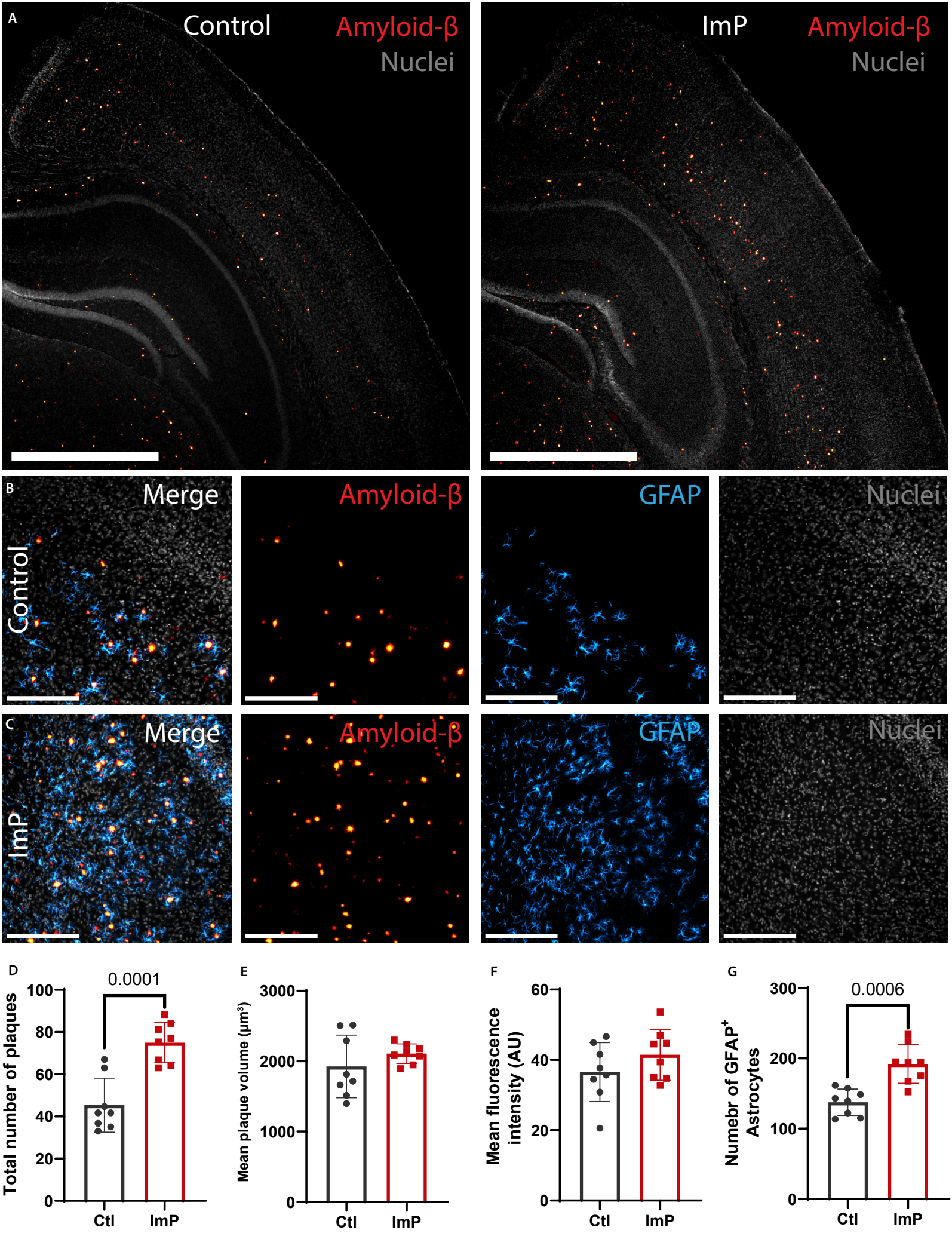
A
Control
Amyloid-β
Nuclei
ImP
Amyloid-β
Nuclei
B
Merge
Amyloid-β
GFAP
Nuclei
Control
C
Merge
Amyloid-β
GFAP
Nuclei
ImP
D
0.0001
Total number of plaques
100
80
60
40
20
0
Ctl
ImP
E
Mean plaque volume (μm³)
3000
2000
1000
0
Ctl
ImP
F
Mean fluorescence intensity (AU)
60
40
20
0
Ctl
ImP
G
0.0006
Numebr of GFAP⁺ Astrocytes
300
200
100
0
Ctl
ImP

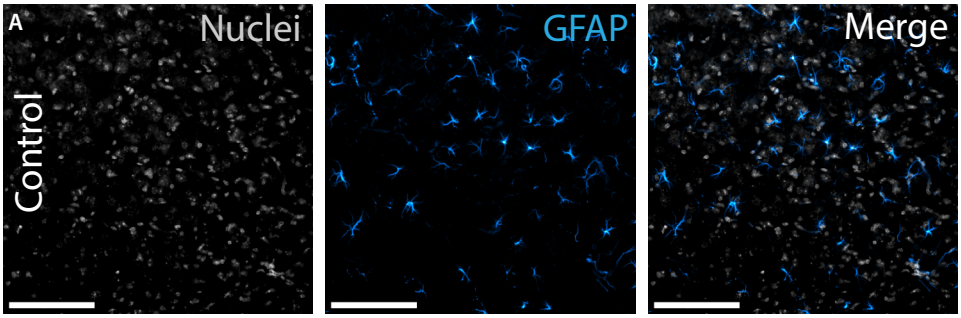
A
Nuclei
GFAP
Merge
Control

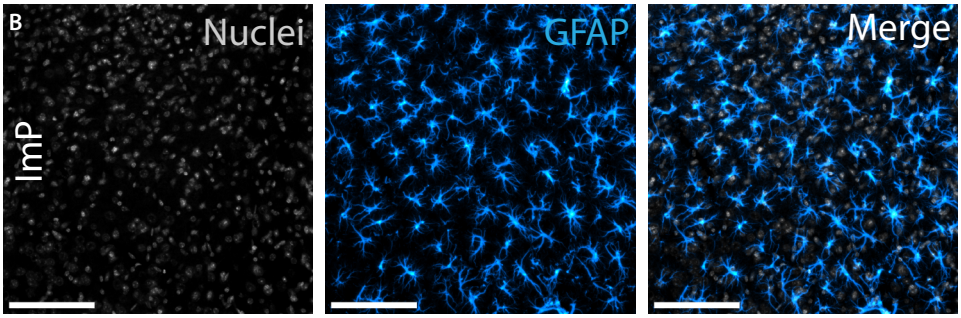
B
Nuclei
GFAP
Merge
ImP

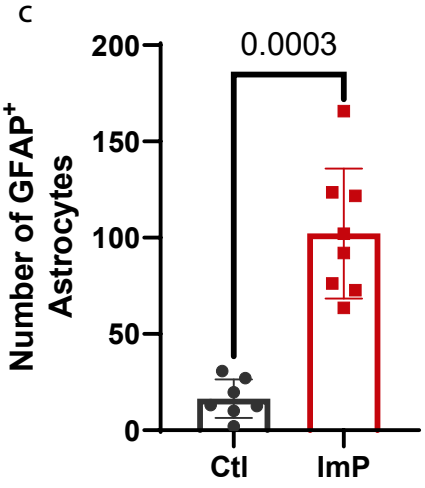
C
0.0003
Number of GFAP+ Astrocytes
200
150
100
50
0
Ctl
ImP

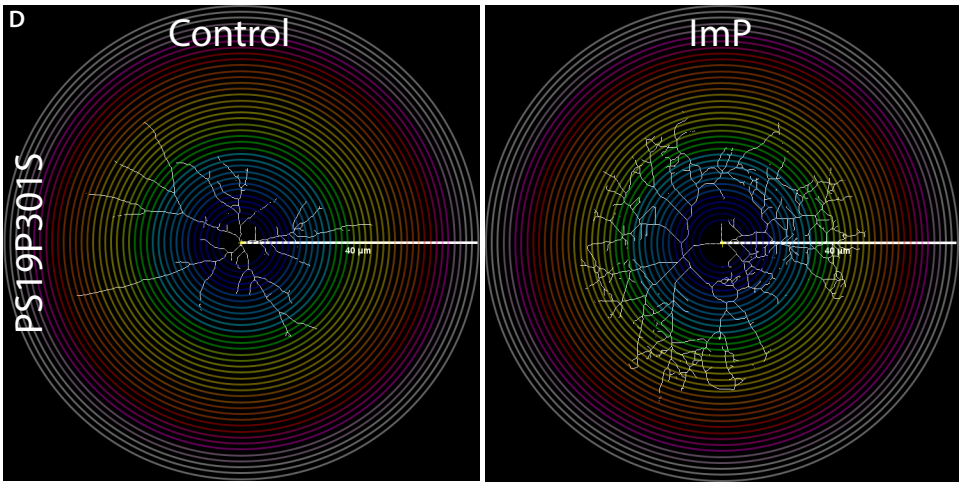
D
Control
ImP
PS19P301S

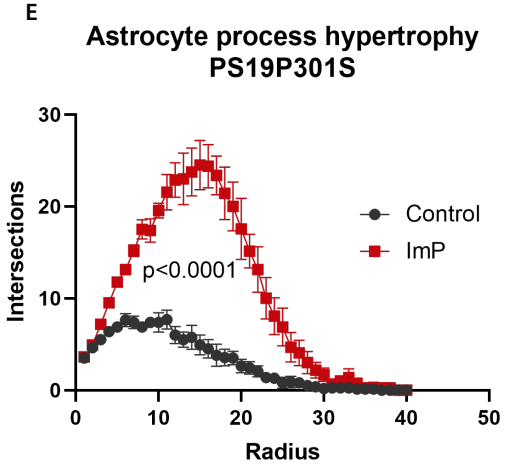
E
Astrocyte process hypertrophy
PS19P301S
Intersections
Radius
Control
ImP
p<0.0001
0
10
20
30
40
50

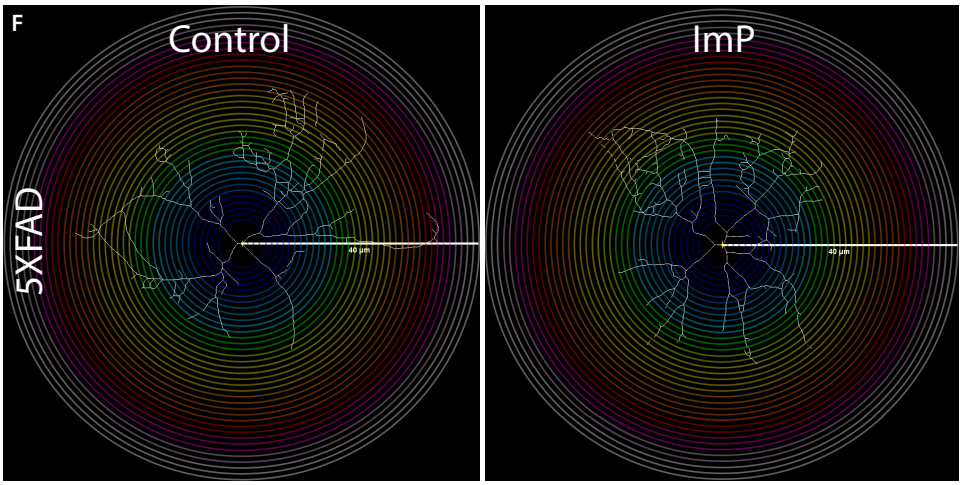
F
Control
ImP
5XFAD

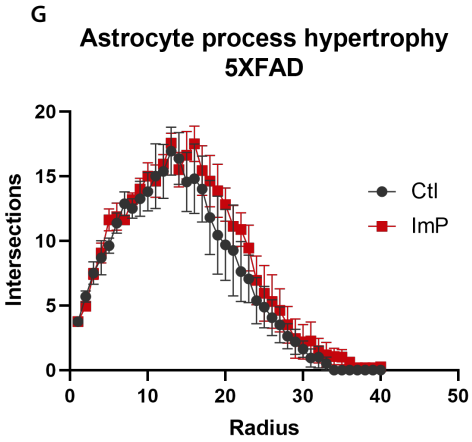
G
Astrocyte process hypertrophy
5XFAD
Intersections
Radius
Ctl
ImP
0
5
10
15
20
30
40
50

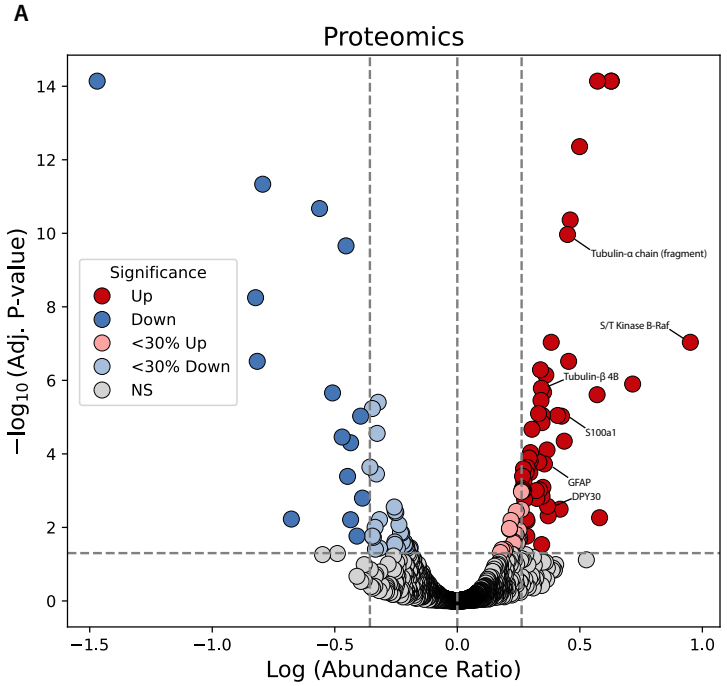
A
Proteomics
Significance
Up
Down
<30% Up
<30% Down
NS
Tubulin-α chain (fragment)
S/T Kinase B-Raf
Tubulin-β 4B
S100a1
GFAP
DPY30
−log10 (Adj. P-value)
Log (Abundance Ratio)

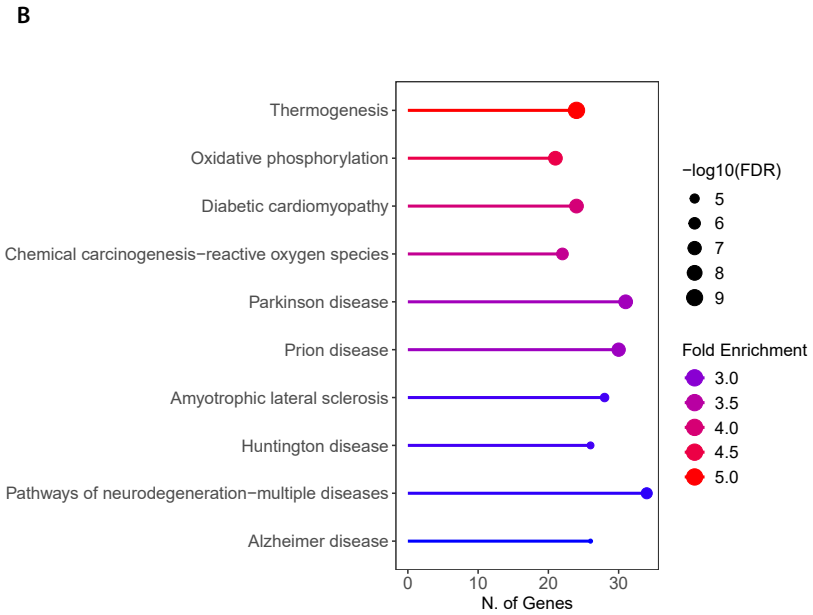
B
Thermogenesis
Oxidative phosphorylation
Diabetic cardiomyopathy
Chemical carcinogenesis−reactive oxygen species
Parkinson disease
Prion disease
Amyotrophic lateral sclerosis
Huntington disease
Pathways of neurodegeneration−multiple diseases
Alzheimer disease
N. of Genes
−log10(FDR)
Fold Enrichment

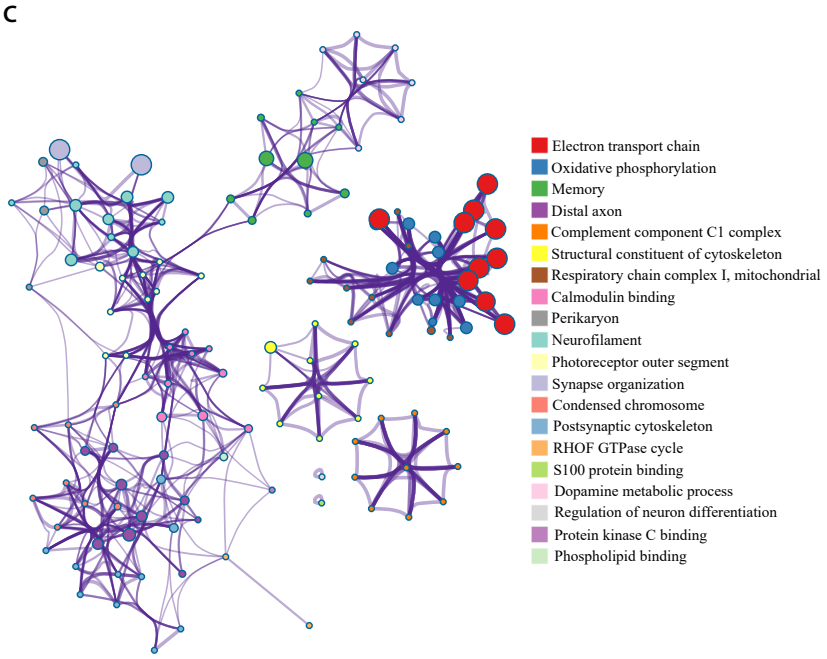
C
Electron transport chain
Oxidative phosphorylation
Memory
Distal axon
Complement component C1 complex
Structural constituent of cytoskeleton
Respiratory chain complex I, mitochondrial
Calmodulin binding
Perikaryon
Neurofilament
Photoreceptor outer segment
Synapse organization
Condensed chromosome
Postsynaptic cytoskeleton
RHOF GTPase cycle
S100 protein binding
Dopamine metabolic process
Regulation of neuron differentiation
Protein kinase C binding
Phospholipid binding

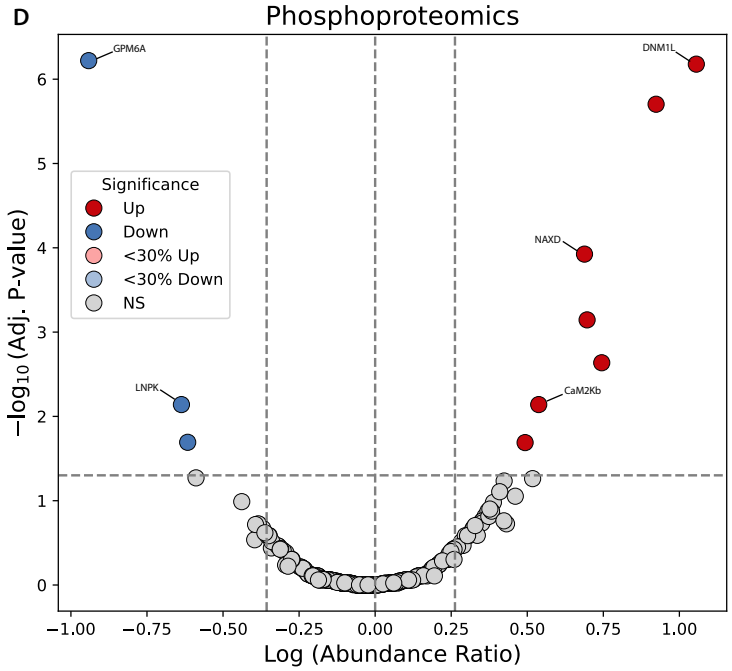
D
Phosphoproteomics
GPM6A
DNM1L
NAXD
LNPK
CaM2Kb
Significance
Up
Down
<30% Up
<30% Down
NS
−log10 (Adj. P-value)
Log (Abundance Ratio)

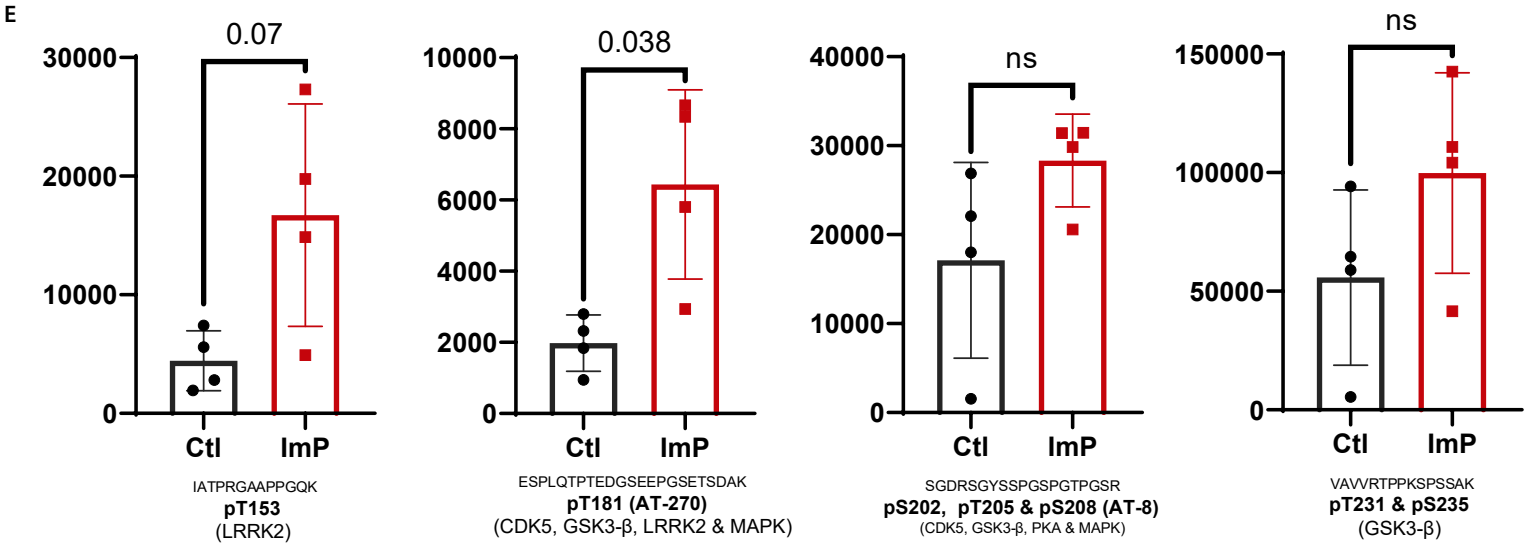
E
0.07
0.038
ns
ns
Ctl
ImP
IATPRGAAPPGQK
pT153
(LRRK2)
ESPLQTPTEDGSEEPGSETSDAK
pT181 (AT-270)
(CDK5, GSK3-β, LRRK2 & MAPK)
SGDRSGYSSPGSPGTPGSR
pS202, pT205 & pS208 (AT-8)
(CDK5, GSK3-β, PKA & MAPK)
VAVVRTPPKSPSSAK
pT231 & pS235
(GSK3-β)

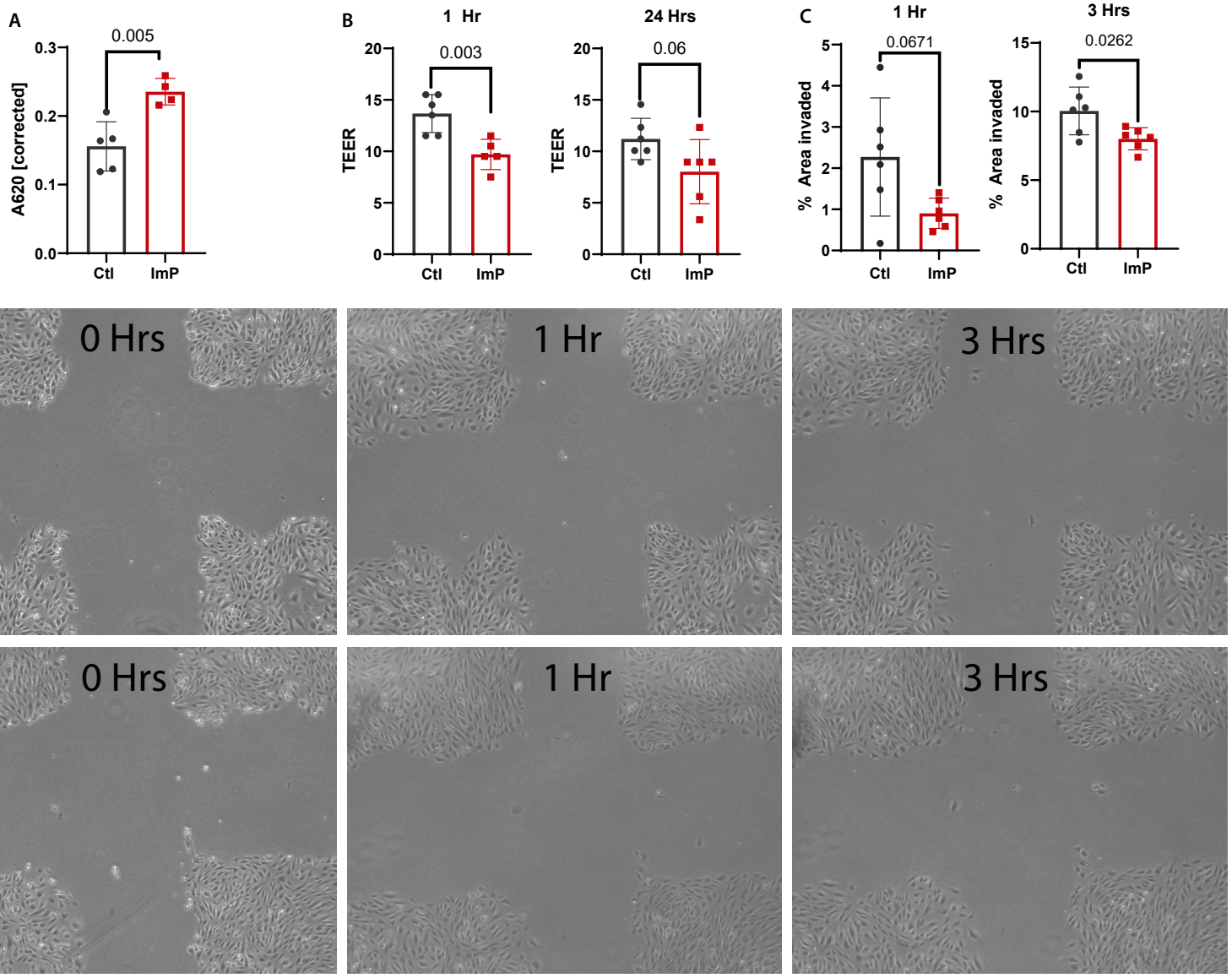
A
0.005
A620 [corrected]
0.3
0.2
0.1
0.0
Ctl
ImP
B
1 Hr
0.003
TEER
20
15
10
5
0
Ctl
ImP
24 Hrs
0.06
TEER
20
15
10
5
0
Ctl
ImP
C
1 Hr
0.0671
% Area invaded
5
4
3
2
1
0
Ctl
ImP
3 Hrs
0.0262
% Area invaded
15
10
5
0
Ctl
ImP
D
0 Hrs
1 Hr
3 Hrs
E
0 Hrs
1 Hr
3 Hrs